Warsaw University of Technology
FACULTY OF PHYSICS

Engineering diploma thesis

on course of applied physics
in specialty of computer physics

Analysis of femtoscopic correlations of proton-antiproton pairs in Pb-Pb collisions at $\sqrt{s_{NN}} = 5.02$ TeV in the ALICE experiment at the LHC

Barbara Chytła
Album number: 311498

supervisor:
Dr Eng. Małgorzata Janik

WARSAW 2024

Abstract

Thesis title: Analysis of femtoscopic correlations of proton–antiproton pairs in Pb–Pb collisions at $\sqrt{s_{NN}} = 5.02$ TeV in the ALICE experiment at the LHC.

By using the femtoscopic technique, it is possible discover the properties of the emission source during an event. In heavy-ion collisions, quark–gluon plasma is produced, thus replicating the state of the early universe. Analysis of two–particle correlations can help in furthering the study of this rare state of matter.

This thesis focuses on analyzing proton–antiproton pairs using data from Pb–Pb collisions at $\sqrt{s_{NN}} = 5.02$ TeV acquired by the ALICE experiment at the LHC. Many studies have been performed on pp femtoscopic correlations, but the baryon–antibaryon interactions remain largely uncharted. Coulomb as well as strong forces play a role, although the latter still yields more impact overall.

Modernisations performed during Long Shutdown 2 allowed for higher energy collisions and better detection technology. Results obtained during the analysis are compared with preliminary correlations from newly taken Pb–Pb collision data as well as previously published ones. HIJING Monte Carlo simulations are used as reference for quality assurance calculations.

Acquired results serve as a baseline for further studies of baryon–antibaryon femtoscopic correlations, providing continuity between run periods and preparing code, as well as reference for future studies.

Keywords:
CERN, ALICE, femtoscopic correlations, heavy–ion collisions

(supervisor’s signature) (student’s signature)

Streszczenie

Tytuł pracy: Analiza femtoskopowa korelacji par proton-antyproton w zderzeniach Pb-Pb o energii $\sqrt{s_{NN}}$ = 5.02 TeV w eksperymencie ALICE na LHC.

Stosując medotę femtoskopową można wydedukować własności obszaru emisji źródła podczas zderzenia. W zderzeniach ciężkich jonów tworzona jest plazma kwarkowo–gluonowa – stan podobny do materii wczesnego wszechświata.

Niniejsza praca skupia się na analizie par proton–antyproton używając danych ze zderzeń Pb–Pb o energii $\sqrt{s_{NN}}$ = 5.02 TeV zebranych przez eksperyment ALICE na LHC. Istnieją liczne badania nad korelacjami par pp, jednak oddziaływania między barionami i antybarionami są znacznie mniej zbadane. Zarówno oddziaływania kulombowskie jak i silne mają znaczący wpływ na korelacje między tymi cząstkami.

Ulepszenia wprowadzone podczas Long Shutdown 2 pozwoliły na kolizje o większych energiach oraz zebieranie znacznie większej ilości danych. Wyniki otrzymane z analizy są porównane z korelacjami otrzymanymi z nowych danych zebranych ze zderzeń Pb–Pb, jak również z wcześniej opublikowanymi wynikami. Symulacje Monte Carlo HIJING użyte są jako punkt odniesienia dla obliczenia jakości próbki danych.

Otrzymane wyniki tworzą podstawę dla przyszłych badań korelacji barion–antybarion, zapewniając ciągłość pomiędzy okresami zbierania danych, rozwijając kod i będąc punktem odniesienia dla kolejnych analiz.

Słowa kluczowe:
CERN, ALICE, korelacje femtoskopowe, zderzenia ciężkich jonów

(podpis opiekuna naukowego) (podpis dyplomanta)

Oświadczenie o samodzielności wykonania pracy

Politechnika Warszawska

Barbara Chytła
311498
Fizyka Techniczna

Oświadczenie

Świadomy/-a odpowiedzialności karnej za składanie fałszywych zeznań oświadczam, że niniejsza praca dyplomowa została napisana przeze mnie samodzielnie, pod opieką kierującego pracą dyplomową.

Jednocześnie oświadczam, że:

- niniejsza praca dyplomowa nie narusza praw autorskich w rozumieniu ustawy z dnia 4 lutego 1994 roku o prawie autorskim i prawach pokrewnych (Dz.U. z 2006 r. Nr 90, poz. 631 z późn. zm.) oraz dóbr osobistych chronionych prawem cywilnym,
- niniejsza praca dyplomowa nie zawiera danych i informacji, które uzyskałem/-am w sposób niedozwolony,
- niniejsza praca dyplomowa nie była wcześniej podstawą żadnej innej urzędowej procedury związanej z nadawaniem dyplomów lub tytułów zawodowych,
- wszystkie informacje umieszczone w niniejszej pracy, uzyskane ze źródeł pisanych i elektronicznych, zostały udokumentowane w wykazie literatury odpowiednimi odnośnikami,
- znam regulacje prawne Politechniki Warszawskiej w sprawie zarządzania prawami autorskimi i prawami pokrewnymi, prawami własności przemysłowej oraz zasadami komercjalizacji.

Warszawa, dnia 20.01.2024 r. (czytelny podpis dyplomanta)

Oświadczenie o udzieleniu Uczelni licencji do pracy

Politechnika Warszawska

Barbara Chytła
311498
Fizyka Techniczna

Oświadczam, że jako autorka pracy dyplomowej pt. *Analiza femtoskopowa korelacji par proton-antyproton w zderzeniach Pb-Pb o energii* $\sqrt{s_{NN}}$ *= 5.02 w eksperymencie ALICE na LHC.* udzielam [1] Politechnice Warszawskiej nieodpłatnej licencji na niewyłączne, nieograniczone w czasie, umieszczenie pracy dyplomowej w elektronicznych bazach danych oraz udostępnianie pracy dyplomowej w zamkniętym systemie bibliotecznym Politechniki Warszawskiej osobom zainteresowanym.

Licencja na udostępnienie pracy dyplomowej nie obejmuje wyrażenia zgody na wykorzystywanie pracy dyplomowej na żadnym innym polu eksploatacji, w szczególności kopiowania pracy dyplomowej w całości lub w części, utrwalania w innej formie czy zwielokrotniania.

Warszawa, dnia 20.01.2024 (czytelny podpis dyplomanta)

[1] Na podstawie Ustawy z dnia 27 lipca 2005 r. Prawo o szkolnictwie wyższym (Dz.U. 2005 nr 164 poz. 1365) Art. 239. oraz Ustawy z dnia 4 lutego 1994 r. o prawie autorskim i prawach pokrewnych (Dz.U. z 2000 r. Nr 80, poz. 904, z późn. zm.) Art. 15a. "Uczelni w rozumieniu przepisów o szkolnictwie wyższym przysługuje pierwszeństwo w opublikowaniu pracy dyplomowej studenta. Jeżeli uczelnia nie opublikowała pracy dyplomowej w ciągu 6 miesięcy od jej obrony, student, który ją przygotował, może ją opublikować, chyba ze praca dyplomowa jest częścią utworu zbiorowego."

Contents

Chapter 1

Introduction

1.1. Heavy ion collisions

High energy heavy ion collisions' main goal is to create an environment in which it is possible to study the properties of quark–gluon plasma (QGP) [1]. It is a state of matter, in which quarks and gluons are deconfined, which means they can move freely and are not bound together into baryons or mesons. Such a state is widely believed to have existed in the first fractions of a second during expansion of the early universe, before formation of more complex particles. It is only possible to recreate it under strict conditions of extreme matter density or temperature. The latter can be achieved by accelerating heavy nuclei stripped of it's electrons, to relativistic velocities and colliding them together. This is the purpose of many particle accelerators of which the Large Hadron Collider (LHC) [2] is the most powerful.

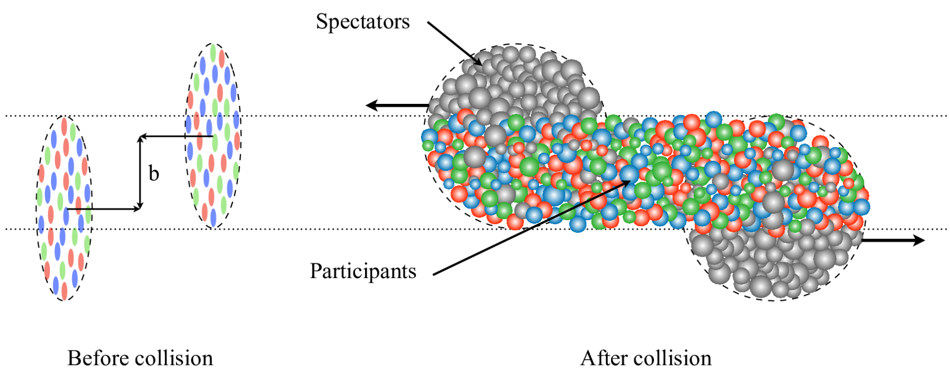

Figure 1.1: Heavy–ion collision [3]

A collision can be divided into several stages. First, when nuclei collide, a QGP "droplet" – a minuscule fireball - is created in the overlap zone between the ions. The size of this region is dependent on the centrality of the event, as the more head-on it is, the more protons and neutrons

interact with each other and fewer become spectators – particles that pass forward mostly unaffected, as illustrated in Fig. 1.1. Afterwards, in the hadronization phase, quarks and gluons merge into particles which later create signal when passing through the detector.
This analysis focuses on protons which consist of two up quarks and one down quark, as well as it's antiparticles – antiprotons made up of two anti–up and an anti–down quark. Both are created in heavy–ion collisions in large quantities.

1.2. Femtoscopy

As it is impossible to directly measure properties of the source, indirect methods are implemented to extrapolate properties of the emission region. Femtoscopy [4] is one such method used to investigate interactions between particles produced in nuclear collisions. It relies on the analysis of relative momenta correlations of two particles created in the same event. A correlation function can be expressed by equation

$$C(p_1,p_2) = \frac{P_2(p_1,p_2)}{P_1(p_1)P_2(p_2)}. \tag{1.1}$$

Femtoscopy describes particle pair correlations in reference to their pair relative momentum k^* given as

$$k^* = \frac{p_1 - p_2}{2} \tag{1.2}$$

where p_1 and p_2 are momenta of each particle. The femtoscopic correlation can be related to the emmission source with the Koonin-Pratt equation [5, 6]

$$C(k^*) = \int S(\vec{r^*}) \left|\Psi_{-\vec{k^*}(\vec{r^*})}\right| d^3\vec{r^*}, \tag{1.3}$$

where $S(\vec{r^*})$ is the source function. It's parameters describe the shape and evolution of the source. When $\left|\Psi_{-\vec{k^*}}\right|$ is known, the femtoscopic technique allows to extract those parameters. It is particularly useful for studying the baryon–antibaryon interaction at low pair relative momenta.
To analyse correlation results in more detail, they can be separated accordingly to relevant parameters like centrality or multiplicity. Centrality classes categorize collisions by the distance between centres of the participating nuclei in the plane transverse to the beam axis and are measured in percentage with 0% being the most and 100% the least central collision. It is directly correlated with event multiplicity N_{ch} which is the quantity characterizing the number of particles created in a collisions. The latter directly depends on event centrality, as more particles are produced in head–on collisions then in peripheral ones. Apart from categorizing by event properties, division in relation to k_T values can also be applied. It which characterises the pair transverse momentum and can be described as

$$k_T = \frac{|p_{T_1} + p_{T_2}|}{2}, \tag{1.4}$$

where p_{T_1} and p_{T_2} are transverse momenta of the correlated particles.

For $p\overline{p}$ pairs, three key effects can be observed. Two of them are Final-State Interactions, which are present in all charged particle correlations – Coulomb and strong forces. As protons and antiprotons are of different charges, therefore not identical, the Fermi–Dirac quantum statistics does not apply. Unlike signed pairs experience Coulomb attraction resulting in a positive correlation at a certain k^* range. Strong interaction also contributes to this tendency. One effect that is unique for particle–antiparticle pairs is annihilation, which results in a negative correlation in low k^* values.

Some non-femtoscopic effects can also be observed in experimental correlation functions. One of them is elliptic flow [7], which describes the nonuniformity of energy and momentum distributions. Although it can be measured and analysed on it's own, it is largely categorized as a background effect when studying femtoscopic correlations.

The analysis of $p\overline{p}$ correlations is a relevant baseline for studies of more exotic systems like $\Lambda\bar{\Lambda}$ [8]. For Λ baryons the pair wave function is not known, but by correlating them with protons and antiprotons their interactions can be studied.

Chapter 2

Experimental setup

2.1. CERN

CERN (Conseil Européen pour la Recherche Nucléaire) [9] is an European organisation that performs research in fundamental particle physics. It operates the biggest particle physics laboratory in the world. The goal of CERN is to explore and better understand the properties of the world around us. The facility consists of many accelerators and decelerators, shown in Fig. 2.1, of which the LHC is the biggest.

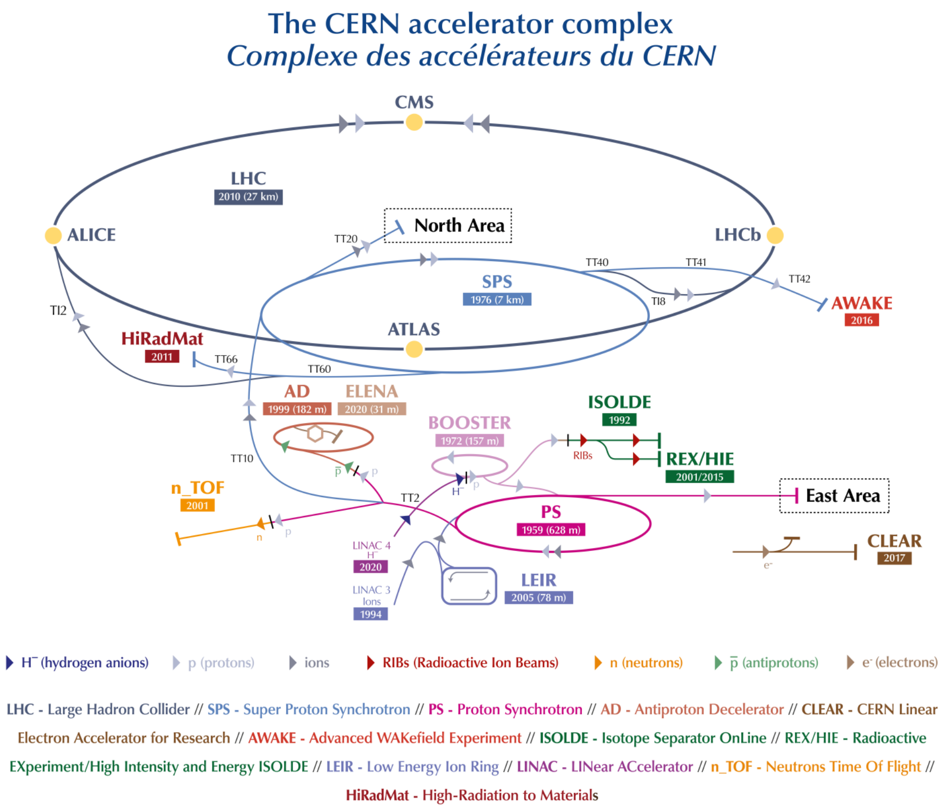

Figure 2.1: The CERN accelerator complex [10]

2.2. LHC

The Large Hadron Collider is the largest and most powerful particle accelerator in the world measuring 27 km in perimeter. It's located between 50 and 175 m underground in France and Switzerland. Four biggest CERN experiments are currently using it to collect data:

- ATLAS (A Toroidal LHC Apparatus) - the largest particle detector in the complex. It's a general-purpose detector particularly known for the discovery of the Higgs boson,
- CMS (Compact Muon Solenoid) - the second general-purpose detector focusing on a wide range of research including studying the Standard Model, and searching for extra dimensions and dark matter,
- LHCb (Large Hadron Collider beauty) - specializes in studying the interactions of heavy hadrons containing a beauty quark in order to measure the difference between matter and antimatter,
- ALICE (A Large Ion Collider Experiment) - focuses on studying heavy–ion collisions and measuring properties of the QGP (Quark–Gluon Plasma).

2.3. ALICE

ALICE [11] is one of the biggest experiments located at the LHC. It's a particle detector, visible in Fig. 2.2, which mainly focuses on heavy–ion physics. The goal of its research is to create quark–gluon plasma - a very dense state of matter, that is supposed to have existed shortly after the Big Bang. Every year, the LHC collides lead ions, recreating an environment similar to that right after the Big Bang. Under these extreme conditions, quarks and gluons are no longer bound together in a nearly free state. The experiments highly advanced laboratory, allows scientists to further study its properties.

During the Second Long Shutdown (LS2) [12] in 2019-2022 the ALICE detector underwent modernization, preparing it for more precise measurements during LHC Run 3. The changes included major modifications of the TPC (Time Projection Chamber) [13] and complete replacement of the ITS (Inner Tracking System) detector [14].

2.3.1. Inner Tracking System

The ITS (Inner Tracking System) is the innermost detector of ALICE. Its main role is to determine the primary vertex of the collision, track and identify low momentum particles and improve resolution for tracks reconstructed by the TPC. During Run 1 and Run 2 the ITS consisted of three double layers. Two Silicon Pixel Detectors (SPD) in the center, then two Silicon Drift Detectors (SDD), and two Silicon Strip Detectors (SSD) as the outermost layer. During LS2 the detector was replaced and

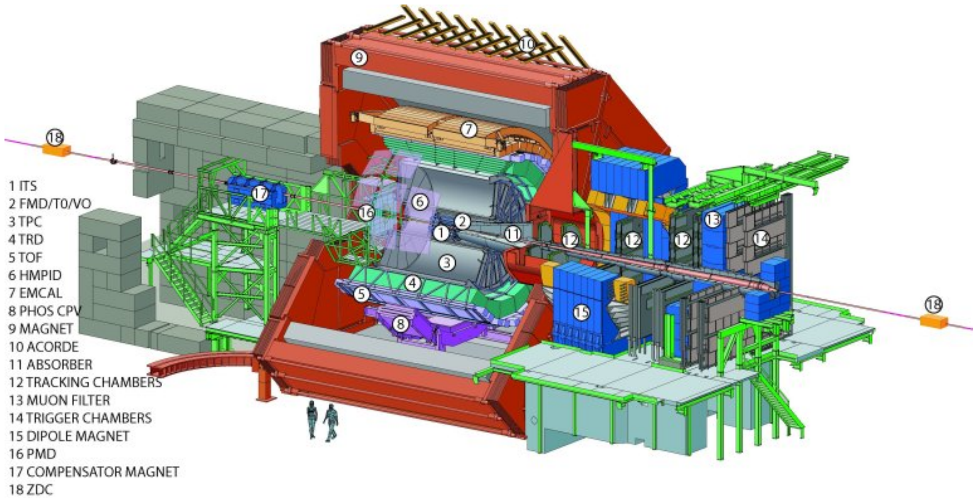

Figure 2.2: Figure from [15]

is now entirely made of 7 layers of monolithic active pixel sensors (MAPS) which provide much higher accuracy, and make it possible to reconstruct tracks based only on ITS signal.

2.3.2. Time Projection Chamber

TPC (Time Projection Chamber) shown in Fig. 2.3, is located between the ITS and TOF and serves as arguably the most important part of the ALICE detector. It consists of a volume of detection compartments filled with gas, in case of ALICE $NeCO_2N_2$ is used. The detector is made out of 159 rows each divided into parts. During a collision, created particles ionise the gas, leaving a trace of activated clusters, allowing for later reconstruction of tracks. The signal from the detector provides the mean energy loss per unit path length. Histograms of those values shown in Fig. 2.4, represent the distribution of measured $\frac{dE}{dx}$ around the value expected from the Bethe-Bloch formula [16]. Their values are a key factor in the particle identification (PID) process.
During the LS2 the TPC detector underwent changes to its data acquisition mode from event based to continuous, to keep up with higher collision rates at the LHC and be able to acquire more data.

2.3.3. Time Of Flight

The main purpose of the TOF (Time Of Flight) [18] detector is registering the time it takes for a given particle to travel from the collision vertex to the point of detection. Together with the TPC detector, it provides valuable information for charged particle identification as well as information necessary to calculate the speed of each particle, while also serving as trigger for cosmic rays and ultraperipheral collisions. ALICE TOF is based on the Multigap Resistive Plate Chamber strip detector segmented into pads for a total of 152928 readout channels, allowing for precise

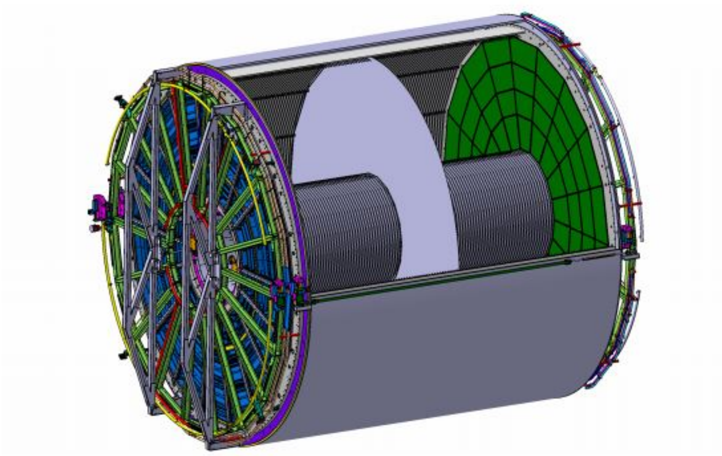

Figure 2.3: The ALICE TPC detector [17].

measurements. Histograms of signal from TOF, as presented in Fig. 2.5, show the distribution of the arrival time around the expected value for each particle.

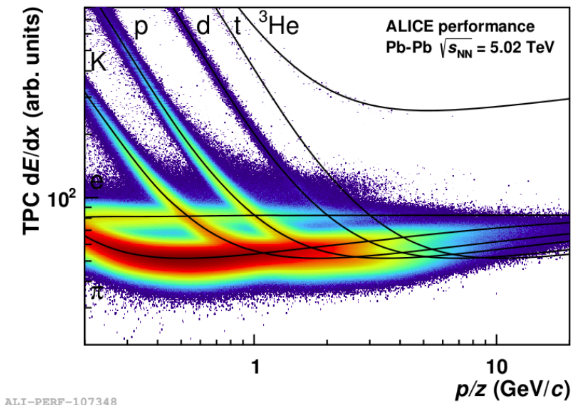

Figure 2.4: The TPC signal as a function of particle momentum [19].

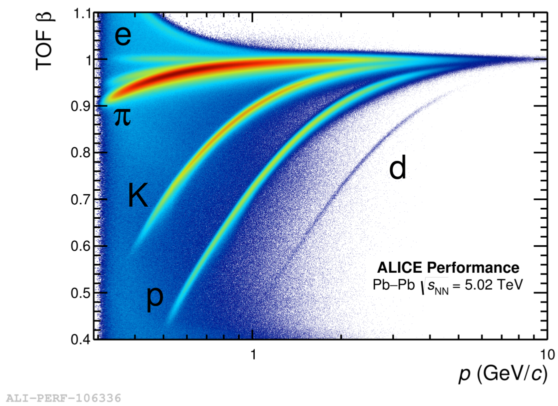

Figure 2.5: The TOF signal as a function of particle momentum [20].

Chapter 3

Software environment

3.1. O^2 framework

One of the changes made during Long Shutdown 2 was an upgrade to the ALICE computing system. Its readout capabilities had to keep up with the increased Pb–Pb collision rates of 50 kHz, which resulted in detector data output exceeding 1 TB/s. The new O^2 data model [21] is designed to reduce the raw data volume as much as possible before relaying it to the O^2 facility. This is achieved by preliminary rapid reconstruction of the data during data taking. This is later followed by a second reconstruction to achieve desired data quality.

To keep up with these changes, a new analysis framework was introduced. It is based on C++ 17 [22] and uses Apache Arrow [23] memory format to store data. The tables used for storage, allow for easy access to each object as well as joining, partitioning and filtering data by its properties. All code developed by ALICE contributors is shared through the Collaboration's GitHub repository [24].

3.1.1. FemtoUniverse

As there are many work groups in ALICE, each focusing on different aspects of particle physics, they have specialized needs when it comes to performing the analysis itself. Each group stores their code in semi–independent packages. FemtoUniverse is one of those, dedicated especially to femtoscopy and angular correlation calculations. Analysis using this package is done in two stages to minimise the data output and overall program run time. The first step uses the Producer task to create derived data called FemtoAO2D. It applies a preliminary selection on the full used dataset and outputs a much smaller data file, which then can be used to run code performing the analysis itself. While there can be multiple specific tasks, they generally use the same Producers, which implies the need for the Producer to be very modular and easily adapt to each selection.

3.1.2. Developed code

As O^2 is constantly being developed, I had to write a portion of my own code, that was needed for my analysis, as well as other future projects. Even though some of the tasks I did are not directly connected to femtoscopy, all contribute in some way to achieving the final analysis results.

A task I worked on, was code for getting quality assurance, data taking efficiency and sample purity plots form Monte Carlo simulated data [25]. As one of the first people, I used it then to perform QA on new MC data from Run 3 pp collisions to help achieve better reconstruction. This program was used in my analysis to calculate proton and antiproton sample purity.

Another objective was adjusting FemtoUniverse to be able to apply binnig in centrality values. Originally code in the whole package focused on analysing pp collision data and as such, used multiplicity tables for event mixing, QA histograms and creating bins for correlations. In case of Pb–Pb collisions, event centrality describes the data in a clearer way and most publications use this kind of selection. I added functions to the FemtoUniverse Producer task, which enable the use of centrality in place of multiplicity for both Run 2 and Run 3 data [26].

Preliminary cut on TOF signal was another addition to the Producer. As it turned out, the derived data output file was very large and running analysis on a full dataset using Hyperloop required too many resources. Cutting out particles, that aren't needed in later parts of the analysis at the stage of the Producer, significantly decreased the derived data size. With the tasks taking fewer resources, I was able to perform analysis on full datasets.

3.2. Hyperloop train system

The Hyperloop [27] is a train system used to perform analysis on the Worldwide LHC Computing Grid (WLCG) [28]. The Grid is a powerful global computing infrastructure enabling access to data produced by the LHC to researchers regardless of their location. Hyperloop users can submit their analysis to the system in form of wagons, which are later joined into trains and run on a specific dataset using the Grid's processing power. The new train system is especially designed to work with the O^2 framework and a direct improvement to it's previous iteration used with AliPhysics [29].

Chapter 4

Data analysis

4.1. Data sample

The analysis was performed on experimental data from Pb-Pb collisions at $\sqrt{s_{NN}}$ = 5.02 TeV taken by the ALICE detector at the LHC and corresponding Monte Carlo simulated data. It was produced during LHC Run 2 in 2015 and 2018 and the simulations use the HIJING Monte Carlo model [30]. The data taken during the 2015 period come from the $LHC15o$ dataset and the 2018 results are combined from two datasets with the same parameters – $LHC18\_PbPb\_q$ and $LHC18\_PbPb\_r$. It is expected, that the 2015 and 2018 datasets do not share the same reconstruction efficiency, therefore they will be analysed separately, as their correlation functions may differ.
The last part of the analysis was performed using newly gathered Pb–Pb collision data from Run 3 at $\sqrt{s_{NN}}$ = 5.36 TeV taken by the ALICE detector and its very first Monte Carlo simulations coming from the PYTHIA 8.3 model [31]. It corresponds to the $LHC23zzh\_pass1$ dataset on Hyperloop and $LHC23k6c\_pass1$ MC dataset. A full list of runs is shown in Appendix A.

4.2. Event selection

To select appropriate events, standard primary vertex and multiplicity cuts were applied as listed in Table 4.1. The ranges for multiplicity are very loose and don't affect the analysis in any significant way other than rejecting faulty data. Event mixing was performed in centrality and multiplicity in different parts of the analysis. Used mixing bins were as follows:

- centrality: 0, 5, 10, 15, 20, 25, 30, 35, 40, 45, 50, 55, 60, 65, 70, 75, 80, 85, 90, 95, 100%,
- multiplicity: 0, 5, 10, 15, 20, 25, 30, 35, 40, 45, 50, 55, 60, 65, 70, 75, 80, 85, 90, 95, 100, 200, 99999,
- z-vertex: -10, -8, -6, -4, -2, 0, 2, 4, 6, 8, 10.

Primary vertex	$\|z\| < 10$ cm
Event multiplicity	$0 < N_{ch} < 32768$

Table 4.1: Event cuts.

4.3. Particle selection

Particle selection cuts are listed in Table 4.2. The same criteria were applied for positive and negative particles. Apart from manually applied selection, the GlobalTrackFilter was used. It is a standard loose set of cuts, implemented into the O^2 framework, that helps select tracks providing reliable data for analysis. GlobalTrackFilter cuts that have been overwritten by a more precise selection, have not been listed in the table.

Applied cuts:	
Pseudorapidity	$\|\eta\| < 0.8$
Transverse momentum	$0.5\,\text{GeV/c} < p_T < 4.0\,\text{GeV/c}$
TPC crossed rows	70
Number of TPC clusters	88
Distance of closest approach XY	$\|DCA_{xy}\| < 2.4\,\text{cm}$
Distance of closest approach Z	$\|DCA_z\| < 2.0\,\text{cm}$
TPC and TOF n_σ	$\|n_{\sigma,TPC+TOF}\| < 3.0$ for $p_T > 0.5 GeV/c$
GlobalTrackFilter cuts:	
Min. ratio of crossed rows over findable TPC clusters	0.8
Max. chi2 per TPC cluster	4.0
Max. chi2 per ITS cluster	36.0
Require TPC refit	True
Require ITS refit	True
ITS cluster requirement	At least one hit in 3 innermost ITS layers

Table 4.2: Proton and antiproton selection criteria.

Particle identification is performed by applying TPC and TOF n_σ selection, which is a cut on the number of standard deviations from the expected value. The formula for the n_σ combined is given by Eq. 4.1:

$$n_{\sigma,TPC+TOF} = \sqrt{n^2_{\sigma,TOF} + n^2_{\sigma,TPC}}. \tag{4.1}$$

Chapter 5

Results

5.1. Quality Assurance

Transverse momentum p_T, pseudorapidity η and azimutal angle φ distributions help estimate the accuracy of corresponding cuts applied. It is expected that there will be less $\bar{p}$ than p for each distribution, as they often annihilate with surrounding matter including secondary particles and the detector itself, yet still the shapes should remain similar for both particles. Fig. 5.1–5.6 show p_T, η and φ distributions for both datasets. The histograms appear clear and correspond to their expected shape, which suggests that the selection is appropriate. Despite the difference in number of entries between the 2015 and 2018 datasets, shapes are very similar.

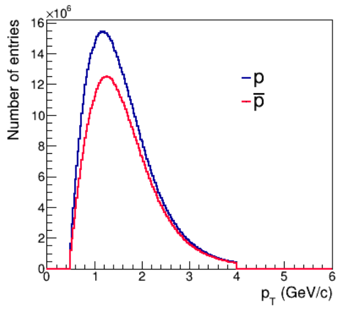

Figure 5.1: Transverse momentum distribution for 2015 data.

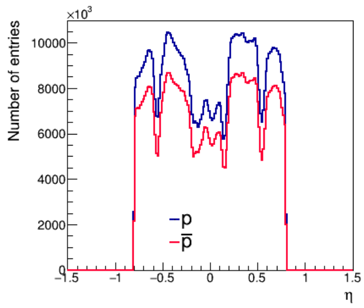

Figure 5.2: η distribution for 2015 data.

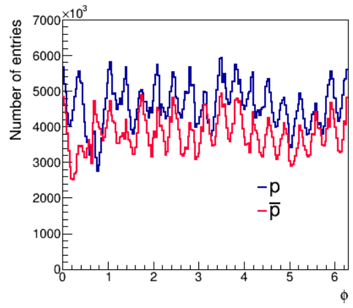

Figure 5.3: φ distribution for 2015 data.

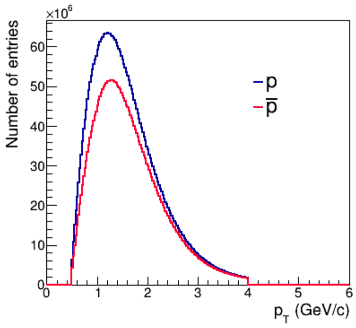

Figure 5.4: Transverse momentum distribution for 2018 data.

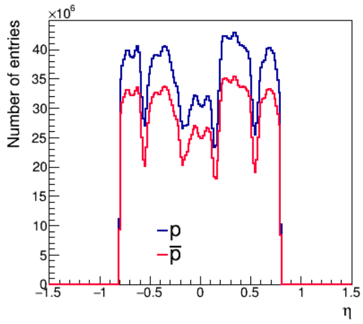

Figure 5.5: η distribution for 2018 data.

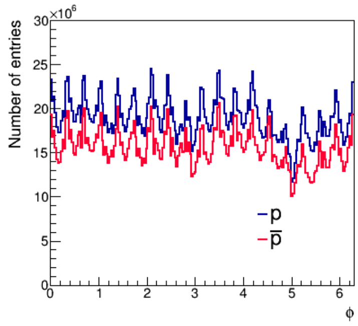

Figure 5.6: φ distribution for 2018 data.

As explained in section 2.3, TPC $\frac{dE}{dx}$ histograms describe energy loss per unit length and help identify particles. The distributions shown in Fig. 5.7–5.10 correspond to the expected shape for protons and antiprotons and are not contaminated by crossing with distributions for other particles. Adequate PID is particularly relevant when studying protons and antiprotons as the are not the most numerous, therefore poor selection will result in distorted results. Most of the contamination comes from kaons, which Bethe–Bloch distributions lie the closest to protons, as well as pions on account of them being the majority of particles created in a collision. Similarly, the TPC and TOF n_σ histograms presented in Fig. 5.13–5.18 appear to be selected properly, although the TPC n_σ distributions are not completely centered at 0, as expected. It is not much of a problem as long as the particles from the peak fall within the considered bounds and aren't cut from the distribution, which appears to be the case. The TOF n_σ histograms used to have an issue with improper storing in the FemtoUniverse data frame, which resulted in them being stretched without a single peak. This was solved by using a table containing full response from TOF. TPC n_σ histograms still use the abridged version of the signal which in the current version of the FemtoUniverse dataframe, have improperly defined bins, causing the strange "stripes" in the histograms.

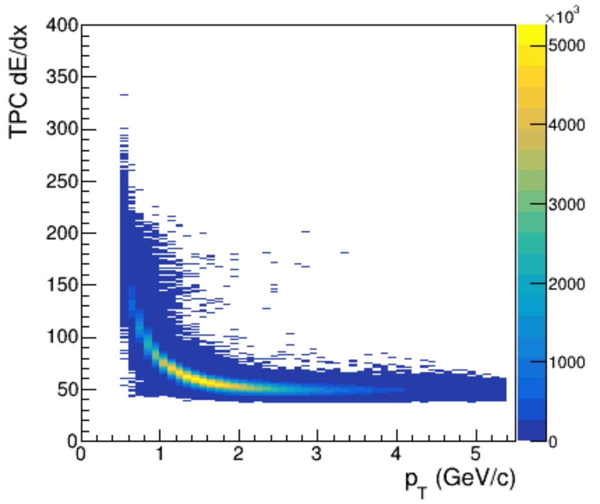

Figure 5.7: The TPC signal as a function of transverse particle momentum for p from 2015 data.

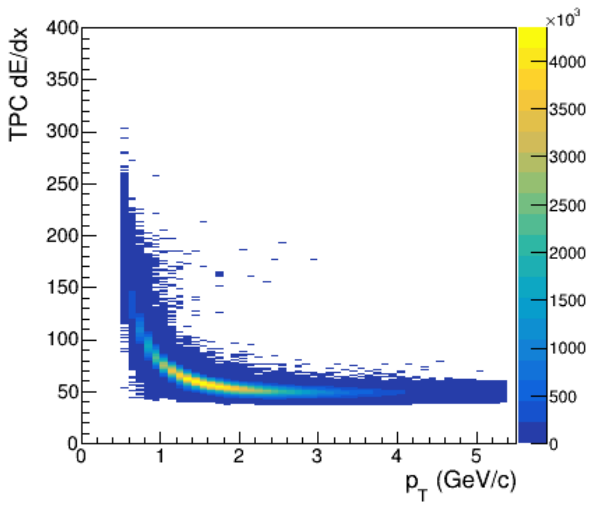

Figure 5.8: The TPC signal as a function of transverse particle momentum for $\bar{p}$ from 2015 data.

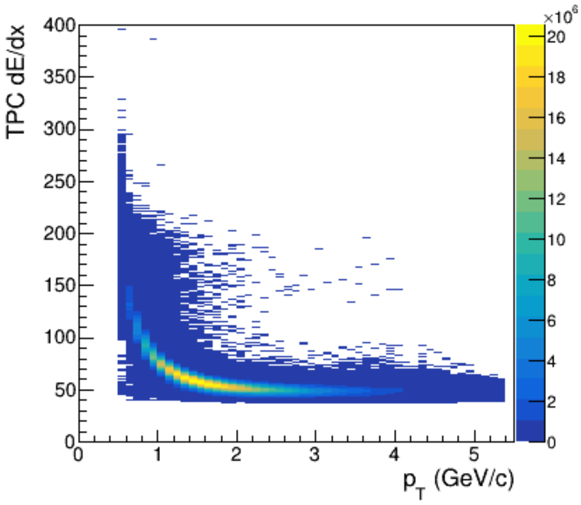

Figure 5.9: The TPC signal as a function of transverse particle momentum for p from 2018 data.

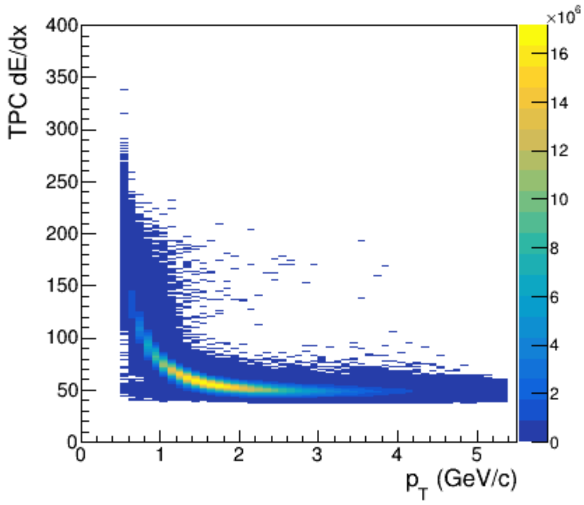

Figure 5.10: The TPC signal as a function of transverse particle momentum for $\bar{p}$ from 2018 data.

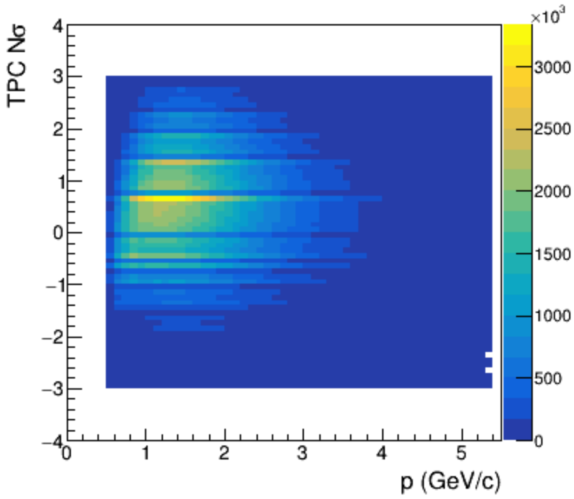

Figure 5.11: TPC n_σ distribution for p from 2015 data.

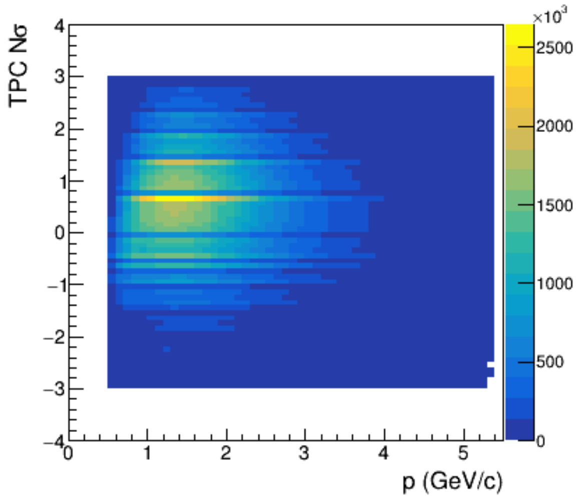

Figure 5.12: TPC n_σ distribution for $\bar{p}$ from 2015 data.

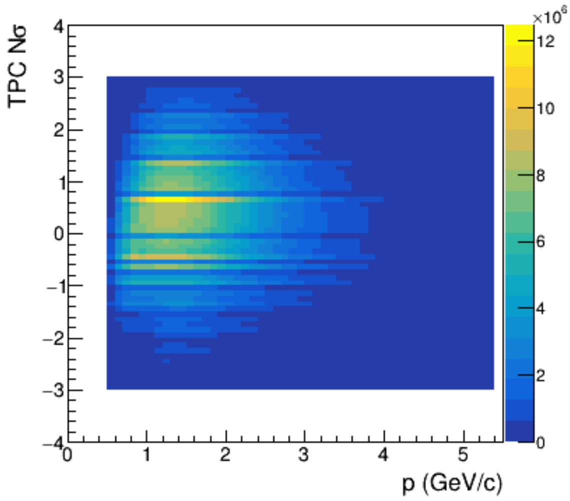

Figure 5.13: TPC n_σ distribution for p from 2018 data.

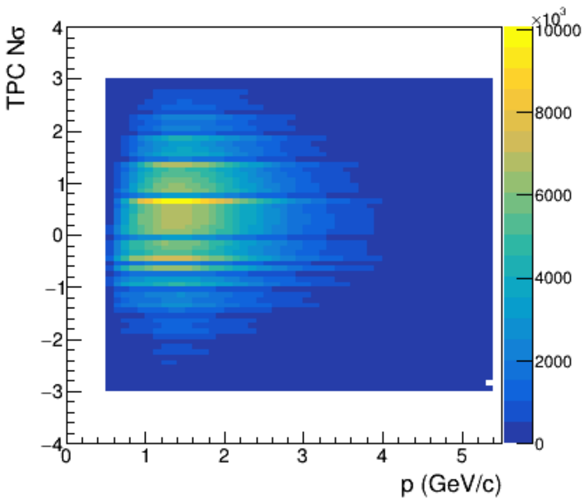

Figure 5.14: TPC n_σ distribution for $\bar{p}$ from 2018 data.

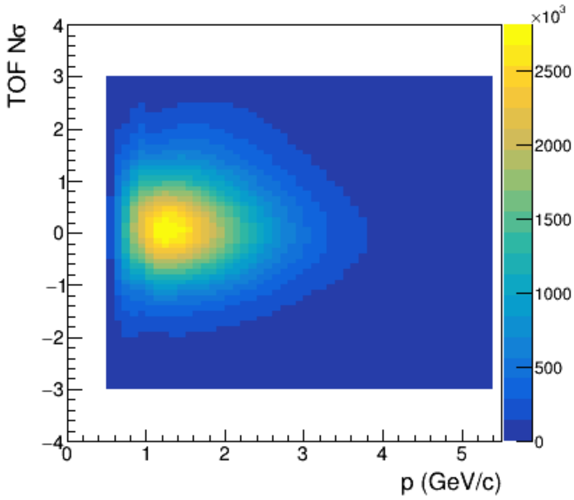

Figure 5.15: TOF n_σ distribution for p 2015 from data.

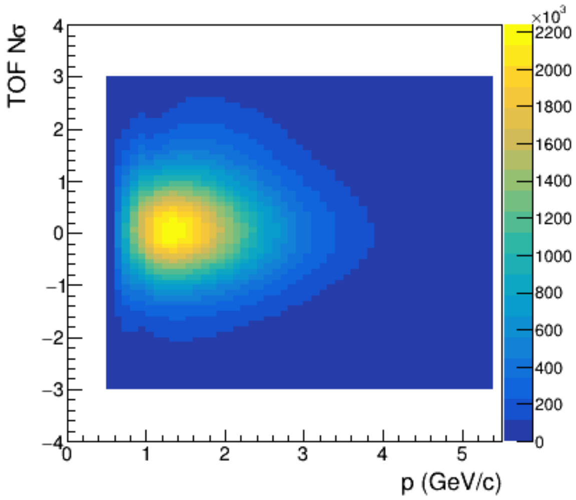

Figure 5.16: TOF n_σ distribution for $\bar{p}$ from 2015 data.

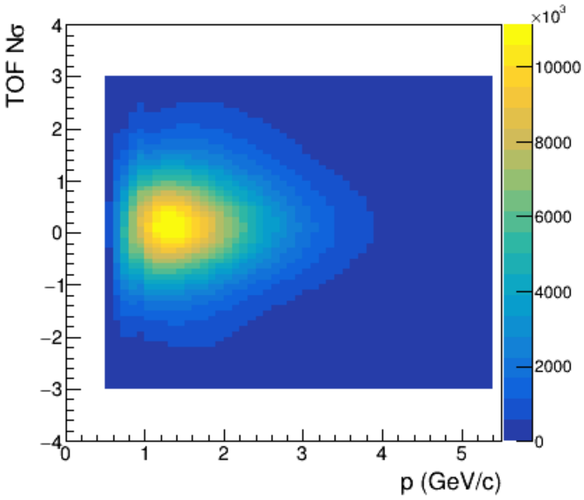

Figure 5.17: TOF n_σ distribution for p 2018 from data.

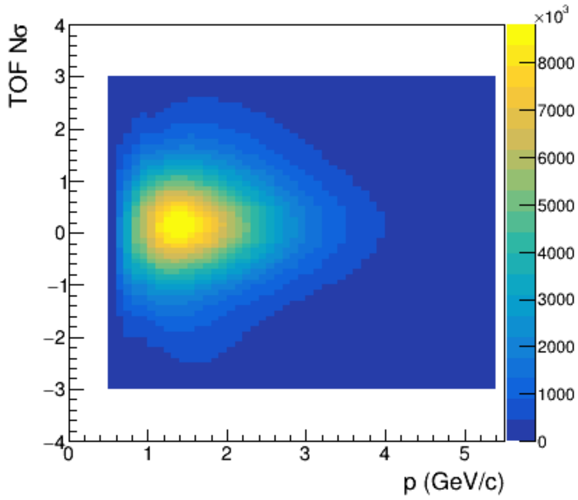

Figure 5.18: TOF n_σ distribution for $\bar{p}$ from 2018 data.

5.1.1. Purity

Data sample purity was calculated using Monte Carlo simulated data. Two datasets were used: LHC20f6 anchored to experimental data from 2015 and LHC20e3c corresponding to 2018 data. Sample purity for both p and $\bar{p}$, with the applied selection is above 95% up to around $p_T = 3\ \frac{\text{GeV}}{c}$, as shown in Fig. 5.19–5.20, which means there is only minimal contamination. Moreover, integrated purity between $0.5 < p_T < 4\ \frac{\text{GeV}}{c}$, presented in table 5.1, is above 98% for the 2015 dataset and over 99% for 2018 data.

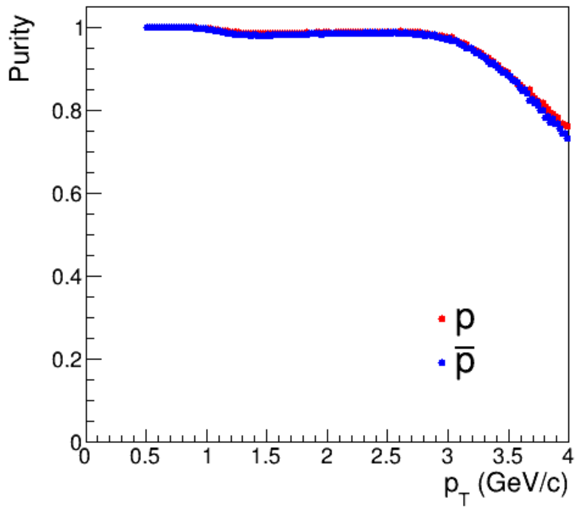

Figure 5.19: p and $\bar{p}$ purity for 2015 data from LHC20f6 MC HIJING simulations.

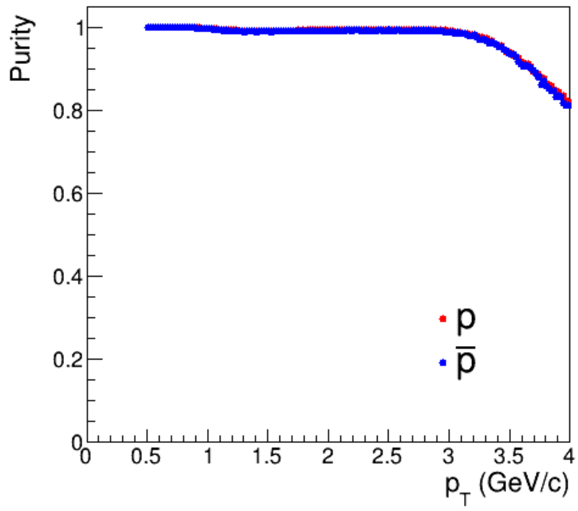

Figure 5.20: p and $\bar{p}$ purity for 2018 data from LHC20e3c MC HIJING simulations.

	p purity	$\bar{p}$ purity
2015 dataset	98.84%	98.60%
2018 dataset	99.38%	99.26%

Table 5.1: Integrated purity.

5.1.2. Centrality and multiplicity distributions

In Fig. 5.21 and Fig. 5.22 are presented event centrality distributions. In O^2, centrality values are calibrated up to 90%, where there can be seen a lack of entries in the histograms. Unfortunately, the calibration in the framework is still imperfect and too many collisions fall into the last bin at 100-105%. This is yet to me solved, that's why an alternative analysis in multiplicity has been performed for reference. As shown in Fig. 5.23 and Fig. 5.24, multiplicity distributions do not experience the described problem and should provide more accurate results. The difference in shape between the runs comes from used triggers during the 2018 run period.

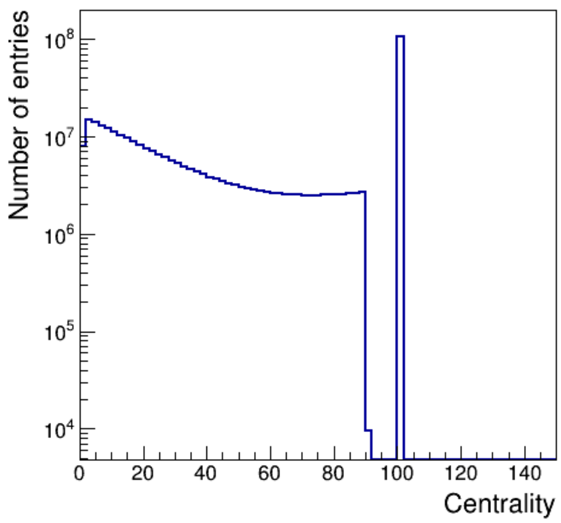

Figure 5.21: Event centrality distribution from 2015 data.

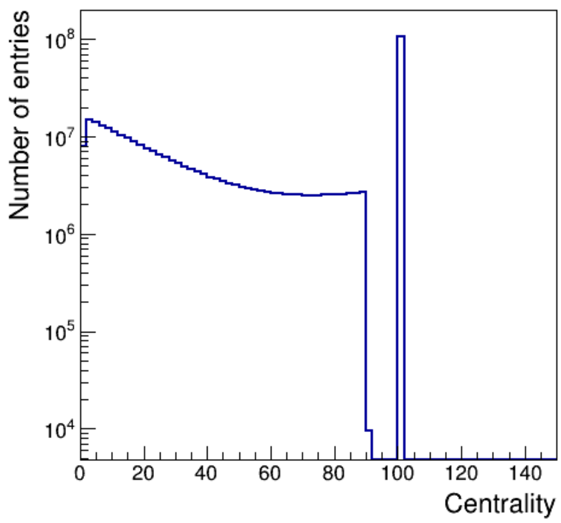

Figure 5.22: Event centrality distribution from 2018 data.

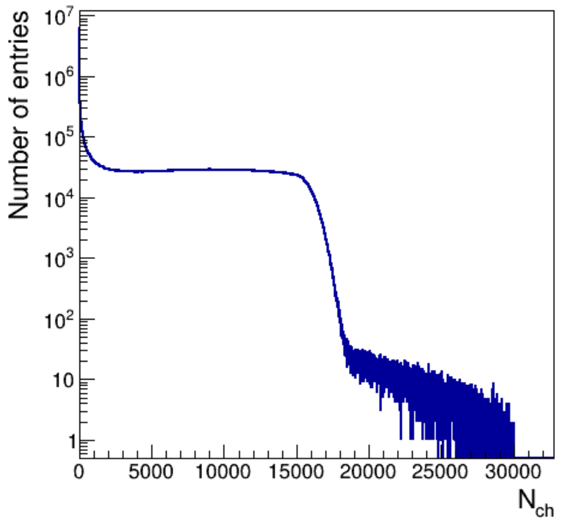

Figure 5.23: Event multiplicity distribution from 2015 data.

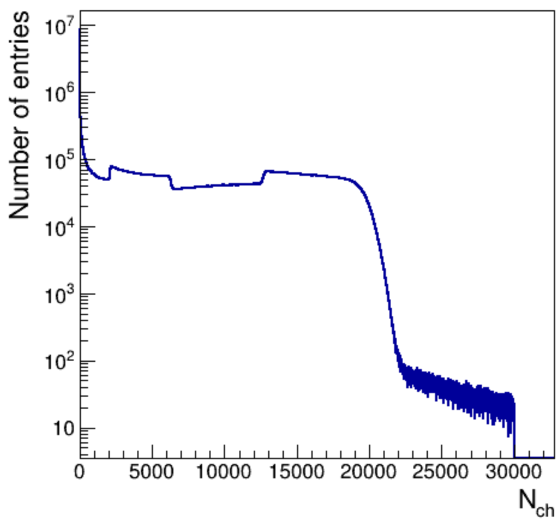

Figure 5.24: Event multiplicity distribution from 2018 data.

5.2. Proton – antiproton correlation functions

5.2.1. Full correlations

The distributions of $p\bar{p}$ pairs from the same and different events, with mixing performed in centrality bins, are presented in Fig. 5.25 and Fig. 5.26. When calculating experimental correlation functions, they are the numerator and denominator. It can be seen that for both datasets, there are more same event pairs than mixed. It is an issue resulting from storing too few collisions in the FemtoUniverse dataframe. Paired with bad centrality reconstruction, there are not enough events which share the same centrality to perform mixing. Apart from that, their general shape is as expected. In Fig. 5.27 and Fig. 5.28 are shown $p\bar{p}$ correlation functions from 2015 and 2018 data, respectively. All presented correlation functions, have been normalized between $0.3 < k^* < 0.4\ \frac{\text{GeV}}{c}$. For both plots, the correlation function falls significantly with lower k^* values due to the annihilation effect. It raises above 1 at the lowest – near $k^* = 0\ \frac{\text{GeV}}{c}$ range which corresponds to the Coulomb attraction between unlike signed particles.

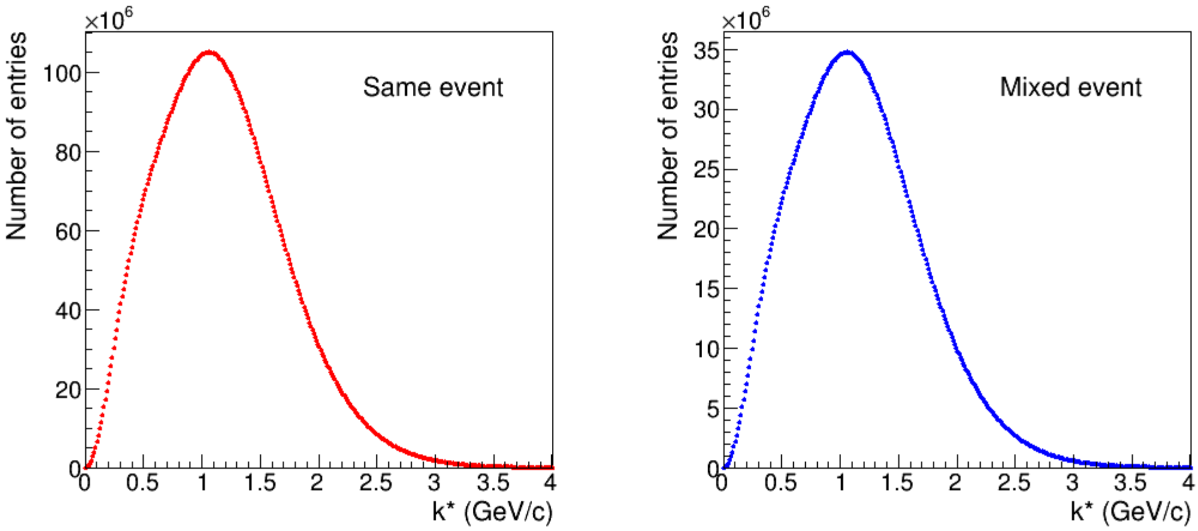

Figure 5.25: $p\bar{p}$ pair distributions with centrality mixing coming from the same and different events from 2015 data.

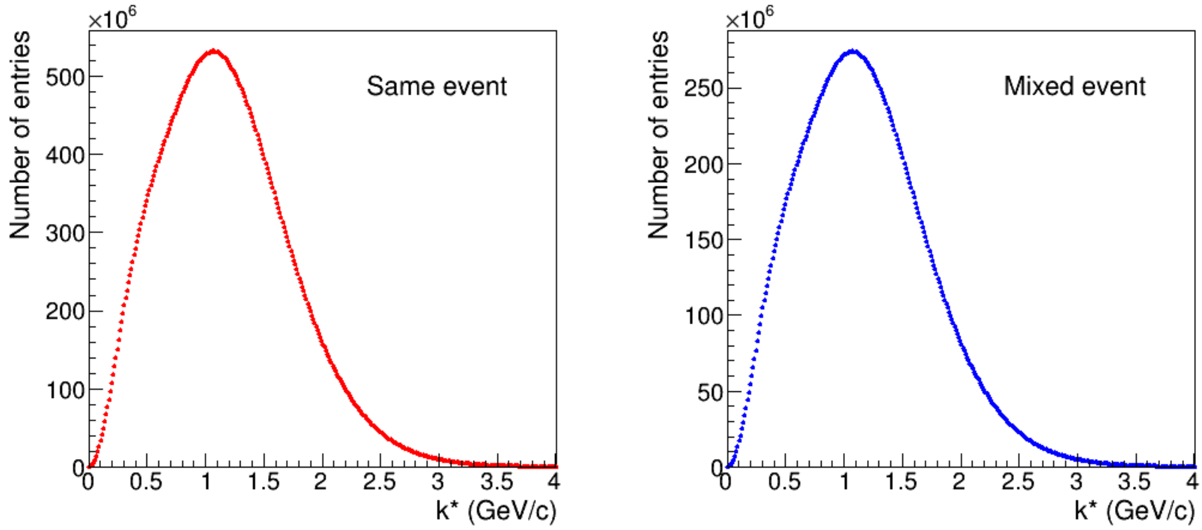

Figure 5.26: $p\bar{p}$ pair distributions with centrality mixing coming from the same and different events from 2018 data.

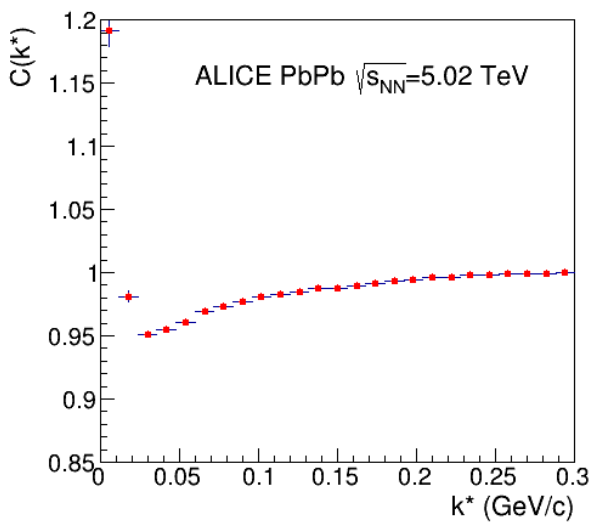

Figure 5.27: $p\bar{p}$ correlation with centrality mixing from 2015 data.

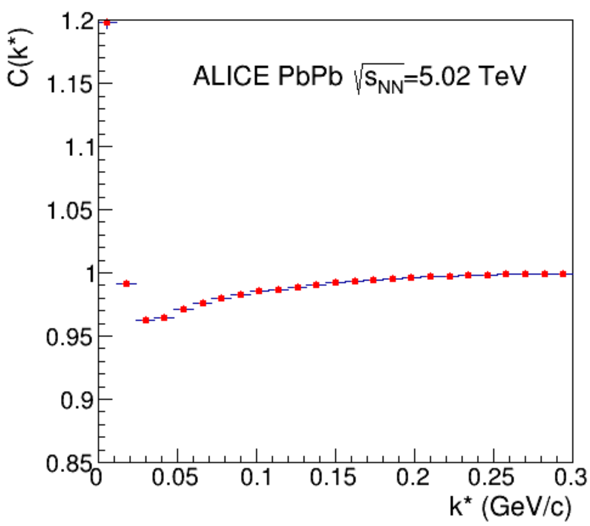

Figure 5.28: $p\bar{p}$ correlation with centrality mixing from 2018 data.

In Fig. 5.29 and Fig. 5.30 are shown pair distributions with mixing in multiplicity bins. They have the same shape as centrality ones, but more entries from mixed events. Correlations with multiplicity mixing are shown in Fig. 5.31 and Fig. 5.32. They have very similar properties only with slightly bigger anticorrelation visible for the 2015 dataset with multiplicity mixing.

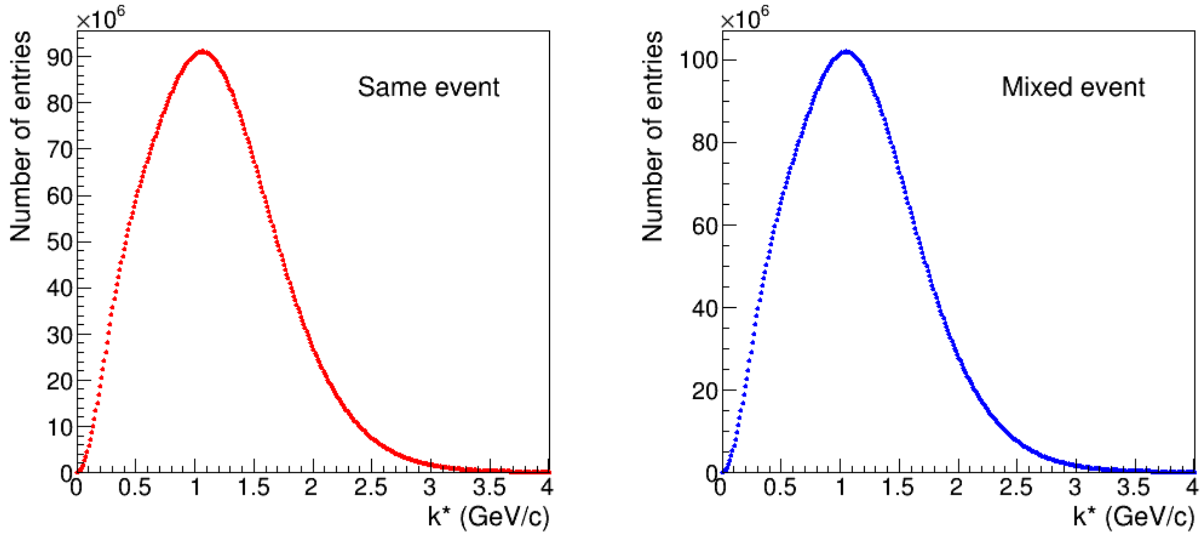

Figure 5.29: $p\bar{p}$ pair distribution coming from the same and different events with multiplicity mixing from 2015 data.

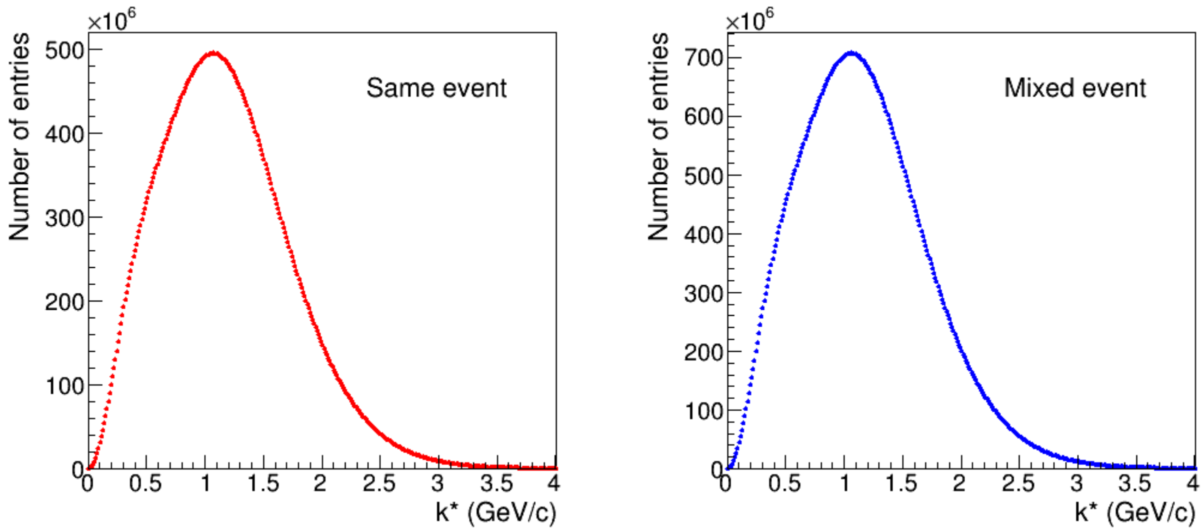

Figure 5.30: $p\bar{p}$ pair distribution coming from the same and different events with multiplicity mixing from 2018 data.

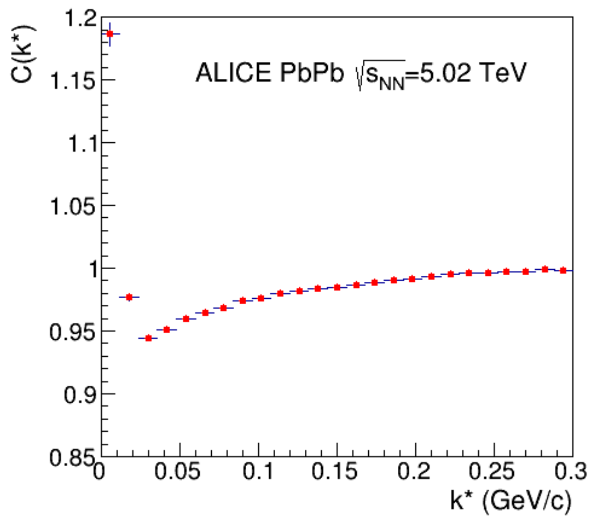

Figure 5.31: $p\bar{p}$ correlation with multiplicity mixing from 2015 data.

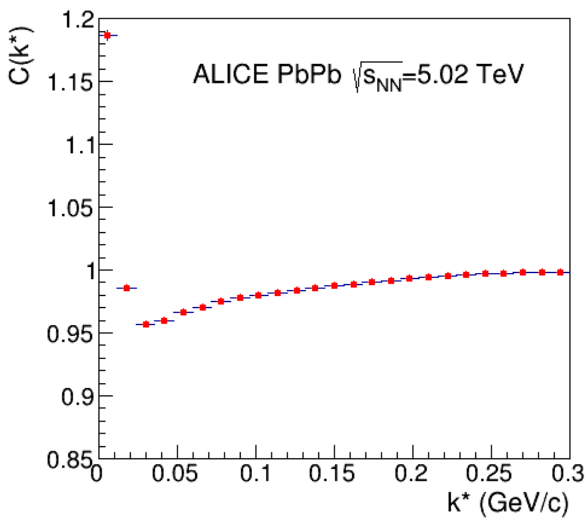

Figure 5.32: $p\bar{p}$ correlation with multiplicity mixing from 2018 data.

5.2.2. Correlations in centrality and k_T bins

Analysis was performed in seven centrality bins: 0 – 5%, 5 – 10%, 10 – 20%, 20 – 30% 30 – 40%, 40 – 50%, 50 – 100% and results were merged into four centrality classes: 0 – 10%, 10 – 30%, 30 – 50%, 50 – 100% in order to observe dependence on this parameter, as low statistics forbade using more ranges for correlation analysis. Bins were chosen arbitrarily to be of similar count, based on event centrality distribution. The 50 – 100% range bears by far the least significant results, as peripheral collisions produce the fewest particles and the focus is put on events between 0 – 50% centrality. In O^2, centrality is calculated based on measured multiplicity values. While in Run 2, this information came from the V0 detector, the FIT detector handles this task for Run 3 data, but the reconstruction remains similar [32]. Two k_T ranges were chosen: $0 < k_T < 1.5\,\frac{\text{GeV}}{\text{c}}$ and $1.5 < k_T < 5\,\frac{\text{GeV}}{\text{c}}$ to compare results for lower and higher values. k_T bins were chosen to have similar statistics.
In Fig. 5.33 and Fig. 5.34 correlation dependence on centrality and k_T can be observed. The anticorrelation dip for low k^* values becomes more prominent for lower centralities. Similarly, it decreases further for higher k_T values. Both datasets display this behaviour. The relation seems coherent for all but last centrality class, as for 50 – 100% the anticorrelation is much smaller than for 30 – 50% centrality. Unfortunately, the centrality calibration in O^2 is still imperfect and as such, it is suspected, that too many events fall into the last centrality bin, as is visible in Fig. 5.21 and Fig. 5.22, thus the shape of correlation coming from the least central collisions does not obey the observed rule.

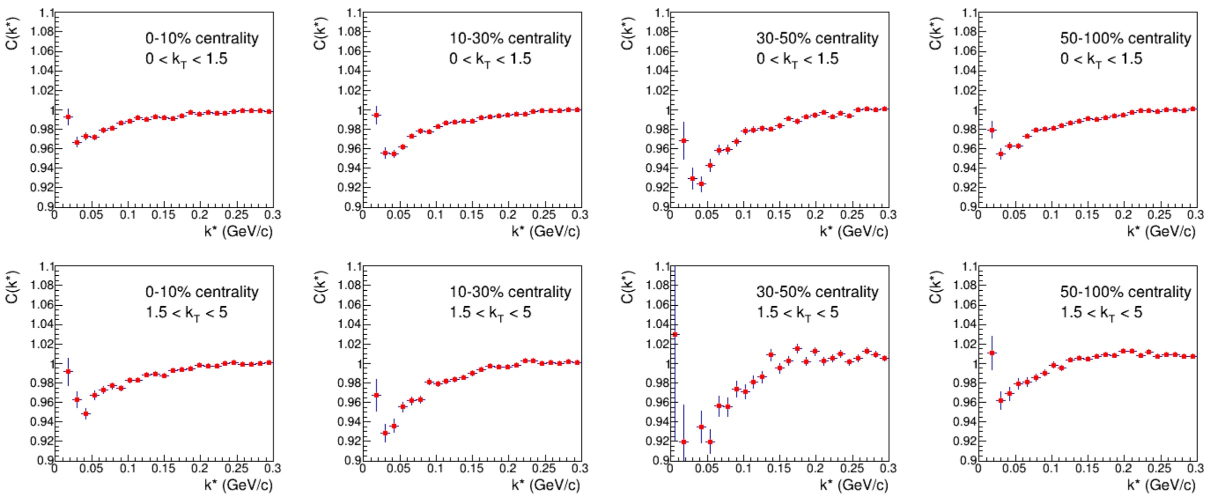

Figure 5.33: $p\bar{p}$ correlation from 2015 data in different centrality and k_T ranges.

In Fig. 5.35 and Fig. 5.36 exact relation between three centrality classes can be seen. Apart from already described behaviour, it is noticeable, that for the $1.5 < k_T < 5\,\frac{\text{GeV}}{\text{c}}$ range the lowest centrality class deviates slightly above the others at $k_* > 0.13\,\frac{\text{GeV}}{\text{c}}$. It is most likely caused by elliptic flow, which effects are more prominent in less central collisions. This effect can be seen in more detail in for a larger k^* range, shown in Fig. 5.45 and Fig. 5.46.

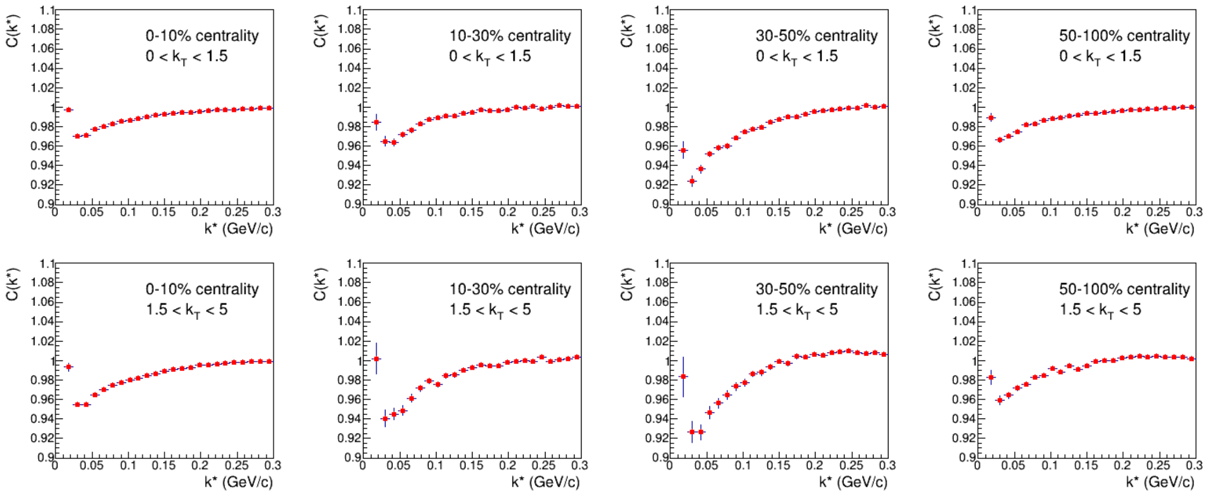

Figure 5.34: $p\bar{p}$ correlation from 2018 data in different centrality and k_T ranges.

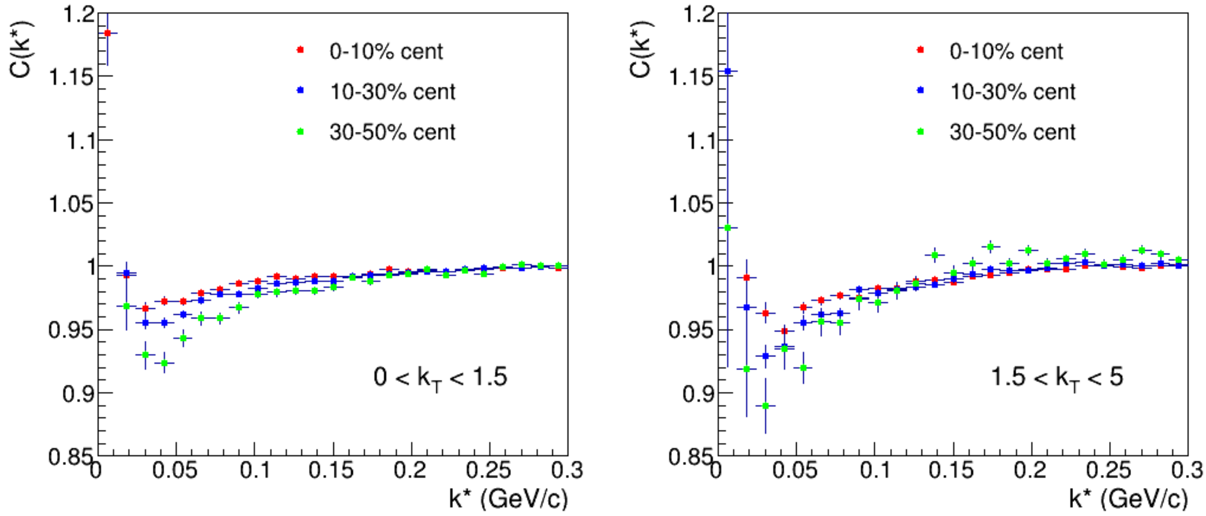

Figure 5.35: $p\bar{p}$ correlation from 2015 data in different centrality and k_T ranges.

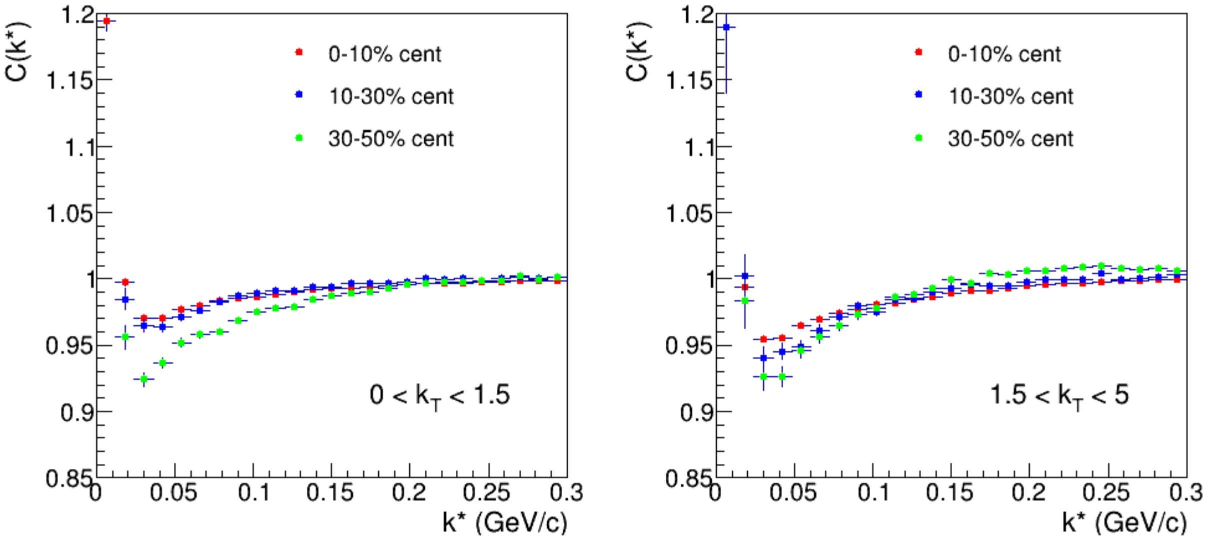

Figure 5.36: $p\bar{p}$ correlation from 2018 data in different centrality and k_T ranges.

5.2.3. Correlations in multiplicity and k_T bins

As centrality dependence may be influenced by the faulty centrality mixing, an analysis in multiplicity ranges have been performed to compare and ensure reasonable results. Seven multiplicity bins have been chosen: 0 – 500, 500 – 1000, 1000 – 2000, 2000 – 4000, 4000 – 7000, 7000 – 10000, 10000 – 30000. Those later have been merged into four multiplicity classes: 0 – 1000, 1000 – 2000, 2000 – 4000 and 4000+. Because of strong flow effects, functions were normalized at $0.2 < k^* < 0.25 \frac{\text{GeV}}{\text{c}}$.
Correlations presented in Fig. 5.37 and Fig. 5.38 display similar k_T dependence as the analysis in centrality bins and the magnitude of the anticorrelation increases for low multiplicities which corresponds to more peripheral events. In Fig. 5.39 and Fig. 5.40 can be seen that for the lowest multiplicity class, the correlation function doesn't decrease more than for the 1000 – 2000 multiplicity range at low k_T values and falls only slightly lower for larger pair transverse momenta. Bins have bin chosen based on multiplicity distribution to contain similar number of events, but do not directly correspond to previously analysed centrality classes.

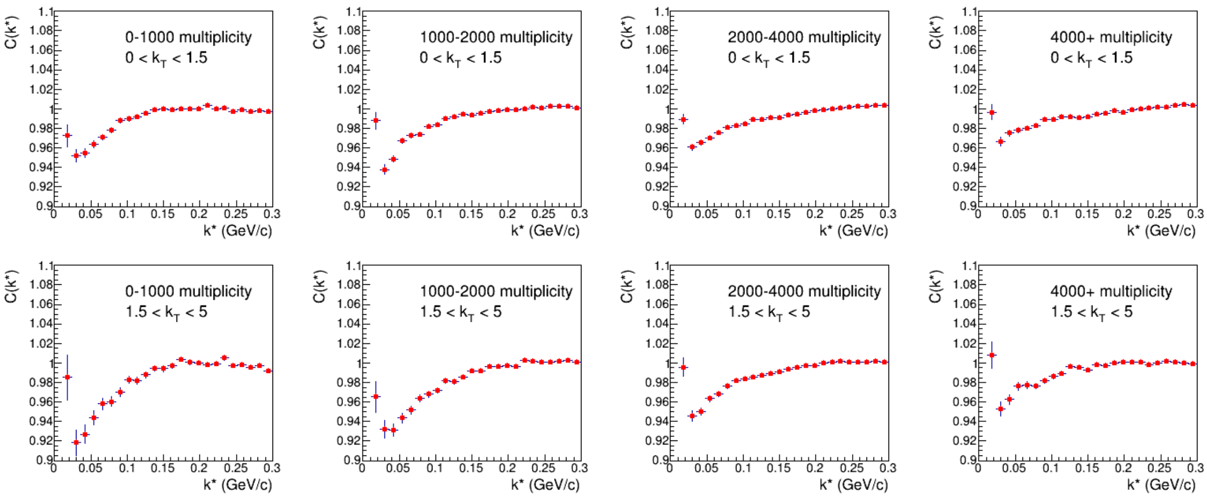

Figure 5.37: $p\bar{p}$ correlation from 2015 data in different multiplicity and k_T ranges.

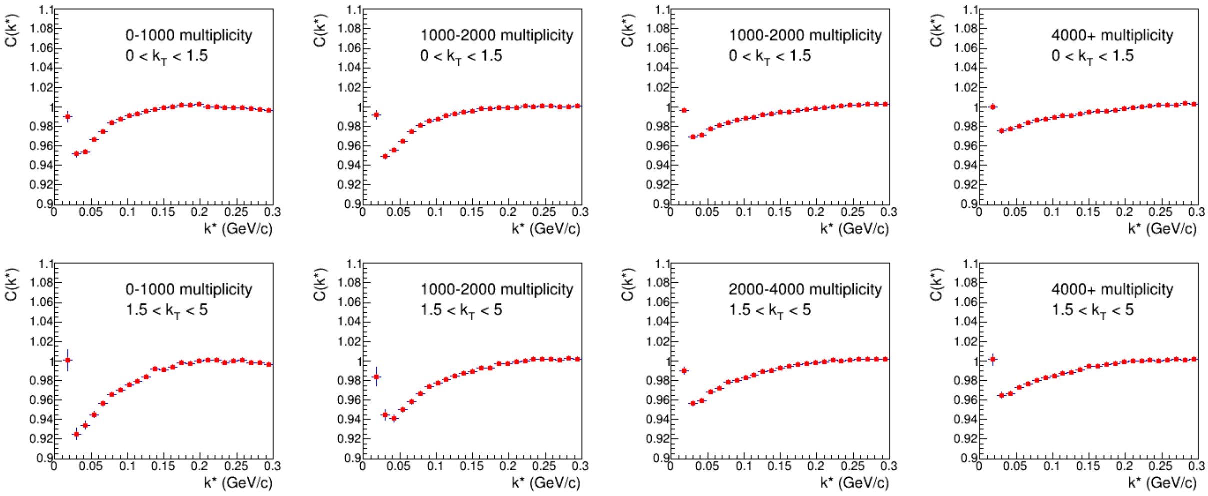

Figure 5.38: $p\bar{p}$ correlation from 2018 data in different multiplicity and k_T ranges.

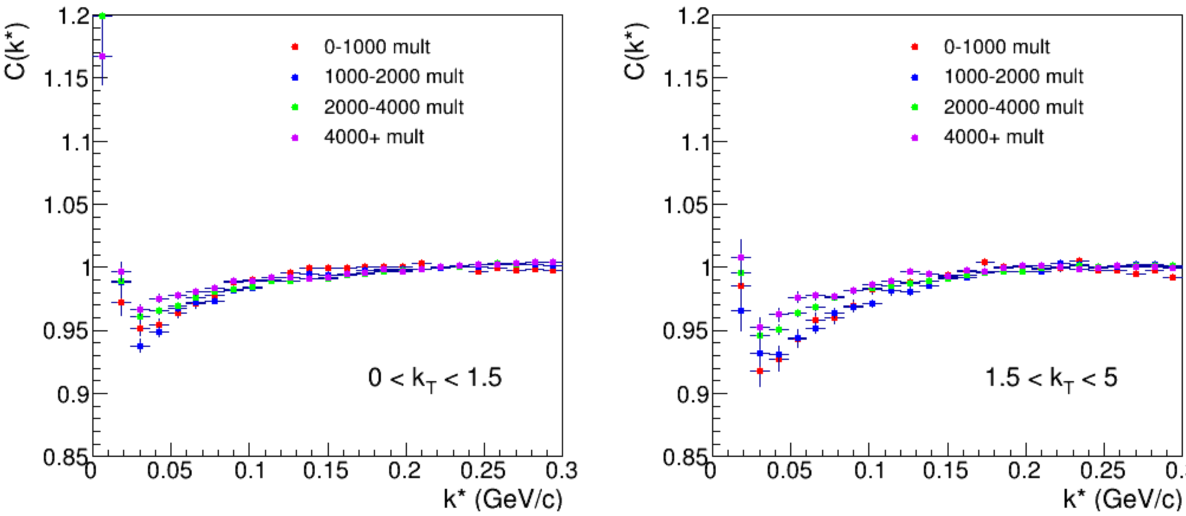

Figure 5.39: $p\bar{p}$ correlation from 2015 data in different multiplicity and k_T ranges.

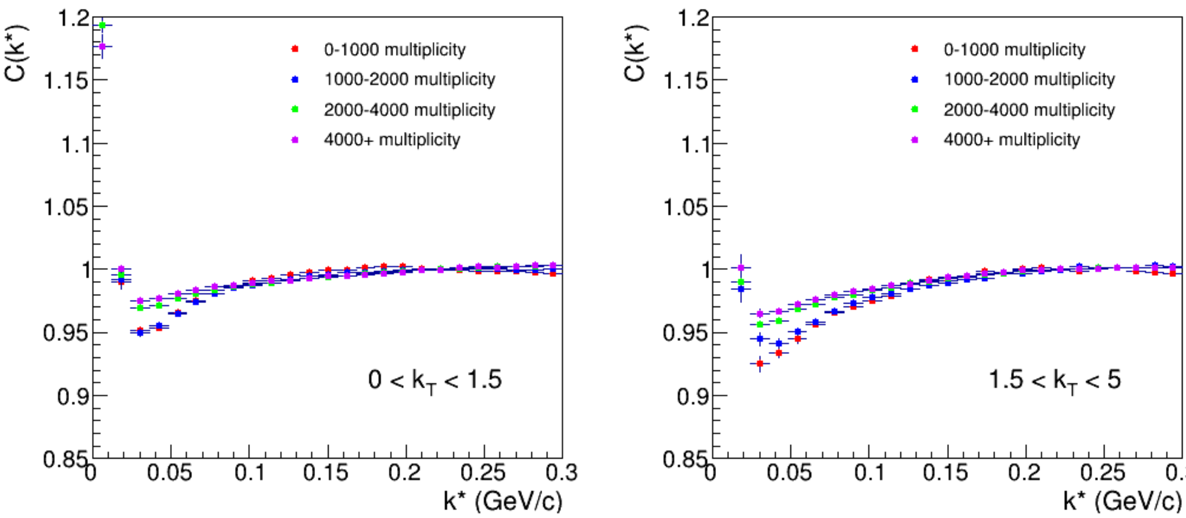

Figure 5.40: $p\bar{p}$ correlation from 2018 data in different multiplicity and k_T ranges.

5.3. Comparison with previous results

$p\bar{p}$ correlations have been studied in ALICE before using the previous framework AliPhysics. In Ref. [8] baryon–antibaryon correlations were analysed with $p\bar{p}$ being reference for $p\bar{\Lambda}$, $\bar{p}\Lambda$ and $\Lambda\bar{\Lambda}$ interactions. In the top part of Fig. 5.41 $p\bar{p}$ correlations are presented for two collision energies at $\sqrt{s_{\mathrm{NN}}}$ = 5.02 TeV and $\sqrt{s_{\mathrm{NN}}}$ = 2.76 TeV at 10 – 20% centrality range. For these results background was subtracted from the correlation functions, although at this low k^* range and high centrality class, non–femtoscopic effects are not very prominent, hence comparison with results from this theses should be accurate. Correlations shown in Fig. 5.42 and Fig. 5.43 were calculated in the same centrality range and with no k_T bins. They are very similar to previously published results with Fig. 5.43 matching the negative correlation dip and Coulomb attraction peak with previous results at $\sqrt{s_{\mathrm{NN}}}$ = 5.02 TeV. This implies that the change of framework did not affect observed physics much, the way it was intended.

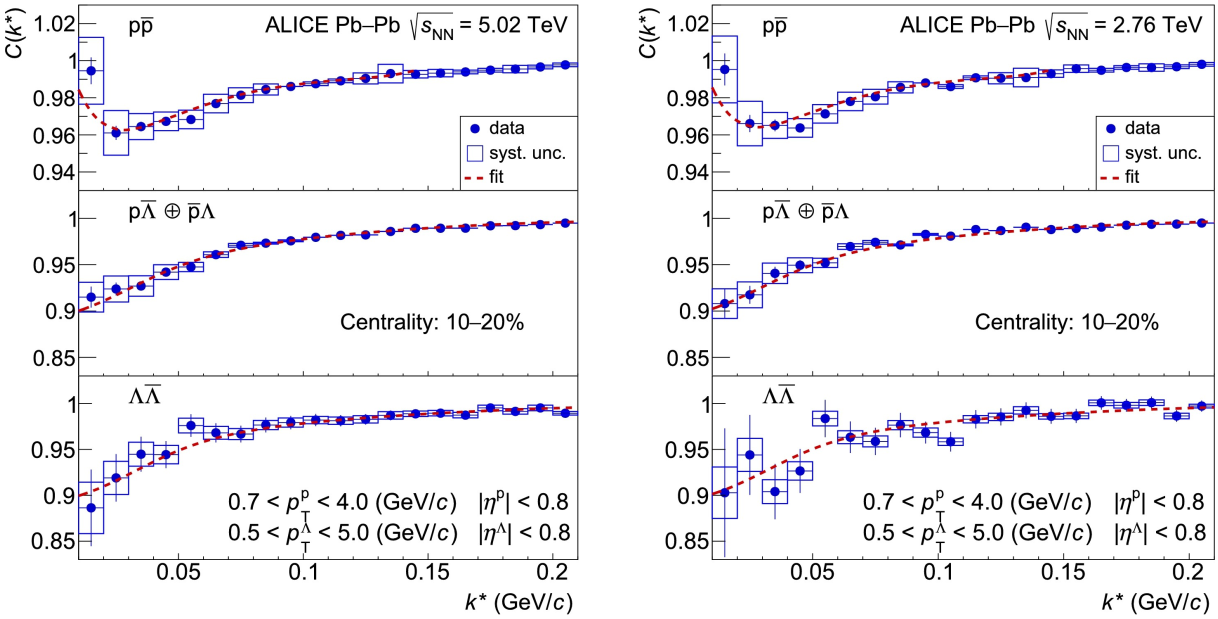

Figure 5.41: $p\bar{p}$ correlation functions for $\sqrt{s_{NN}}$ = 5.02 TeV PbPb collisions at the ALICE experiment [8].

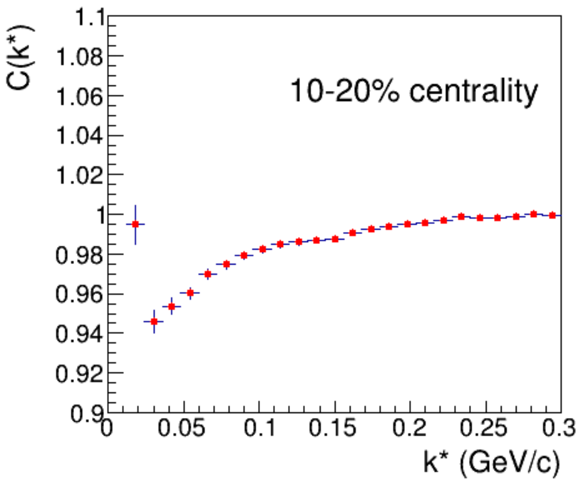

Figure 5.42: $p\bar{p}$ correlation functions at $10-20\%$ centrality for 2015 data at $\sqrt{s_{NN}} = 5.02$ TeV.

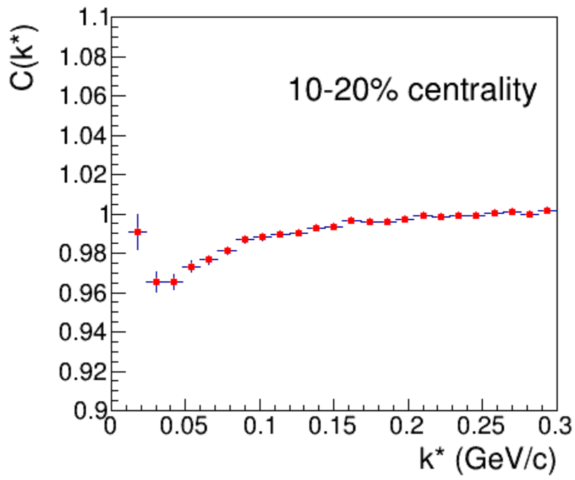

Figure 5.43: $p\bar{p}$ correlation functions at $10-20\%$ centrality for 2018 data at $\sqrt{s_{NN}} = 5.02$ TeV.

In Ref. [33] alongside femtoscopy, the effects of elliptic flow were studied. In Fig. 5.44 are presented results for three centality classes at two k_T ranges: $0.01 < k_T < 1\frac{\text{GeV}}{\text{c}}$ and $1 < k_T < 5\frac{\text{GeV}}{\text{c}}$ at $\sqrt{s_{\text{NN}}} = 2.76$ TeV. In Fig. 5.45 and Fig. 5.46 correlations in the same k^* range are shown. While high centrality events behave very similarly for both energies, less central ones deviate from unity much more at higher energies. The effects of flow are stronger for larger k_T values. For $0 < k_T < 1.5$ for both 2015 and 2018 datasets, the function for the lowest centrality events goes well above 1 at k^* approaching $k^* = 2\frac{\text{GeV}}{\text{c}}$. These differences between previous and current results may also come from the difference in analysed k_T ranges.

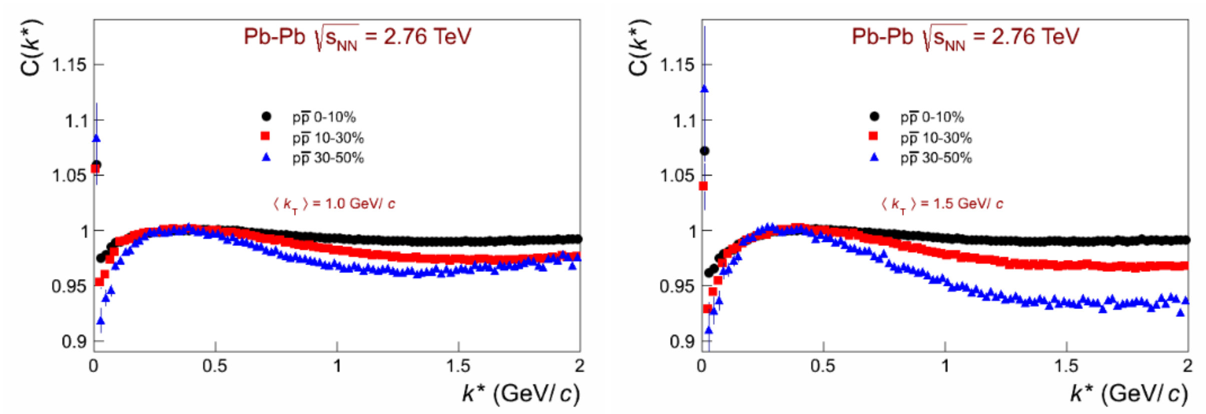

Figure 5.44: $p\bar{p}$ correlation functions for $\sqrt{s_{NN}} = 2.76$ TeV PbPb collisions at the ALICE experiment [33].

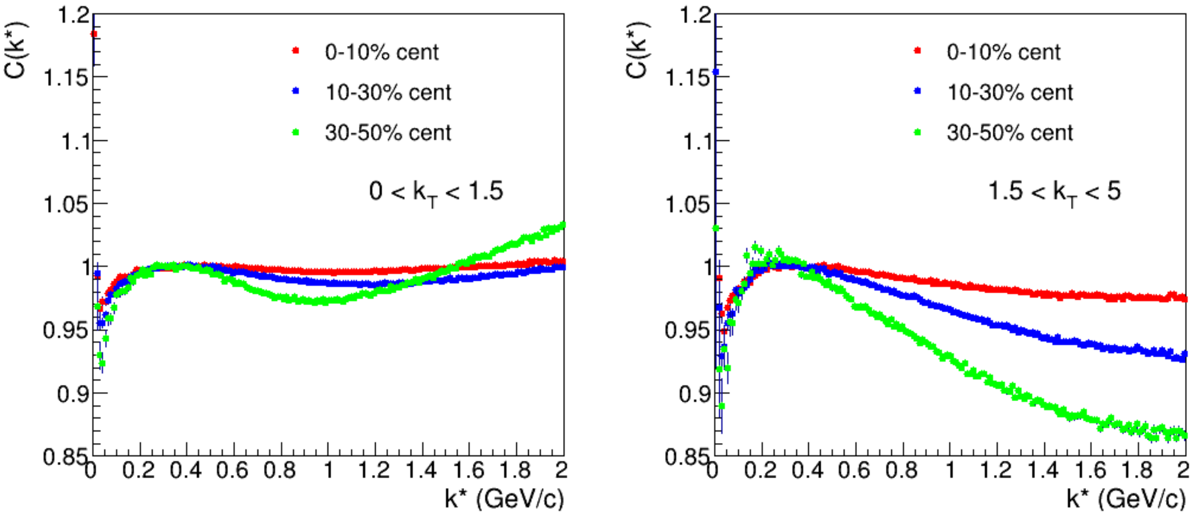

Figure 5.45: $p\bar{p}$ correlation functions at broad k^* range for 2015 data at $\sqrt{s_{NN}}$ = 5.02 TeV.

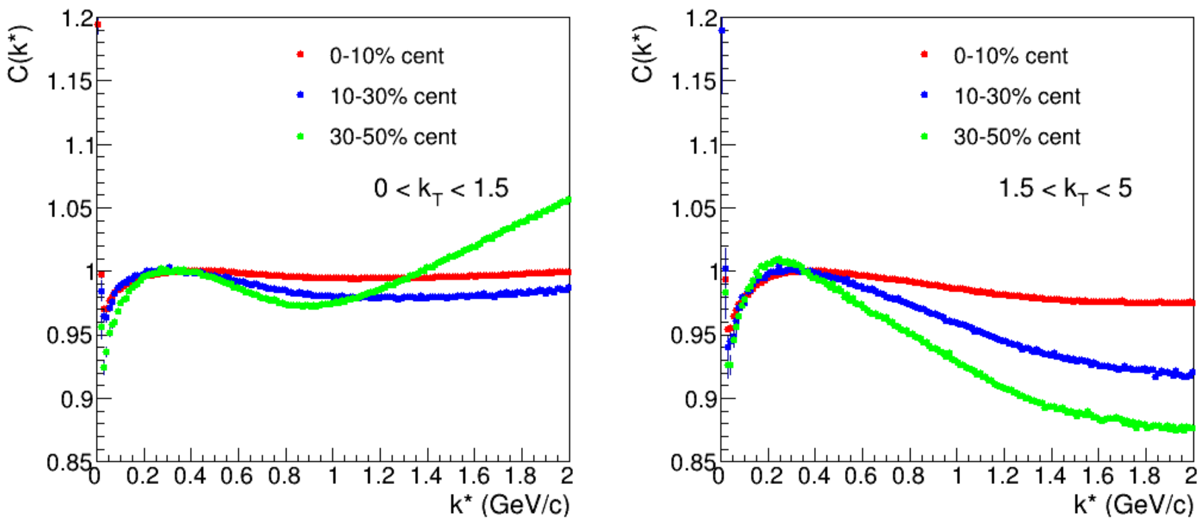

Figure 5.46: $p\bar{p}$ correlation functions at broad k^* range for 2018 data at $\sqrt{s_{NN}}$ = 5.02 TeV.

5.4. Proton–antiproton correlations in Run 3

In September 2023, there was the first datataking period for Pb–Pb collisions in Run 3. A remarkable number of 12 billion collisions has been recorded, dwarfing the amount of data from all previous runs combined. At the time of writing this theses, only limited data from this period is available as it is still being processed to ensure desirable data quality. Nevertheless, it is valuable to look at those first results and compare with previous ones as much as possible. It can be a point of reference pertinent to further study of femtoscopic correlations in Run 3 hinting at possible future results from the new data.

5.4.1. Quality assurance

The transverse momentum distribution presented in Fig. 5.47 appears to be very similar to the results from previous runs only with a more equal numbers of antiprotons compared to protons. It may suggest that more antiprotons are produced, annihilate less with surrounding matter or that there is some contamination present, that changes it's shape. Fig. 5.48 on the other hand, is concave near $\eta = 0$. It is expected that the η distribution should be as uniform as possible, therefore this points a some flaw in pseudorapidity reconstruction. ϕ values shown in Fig. 5.49 fluctuate more than for 2015 and 2018 datasets, but this still can be allowed.

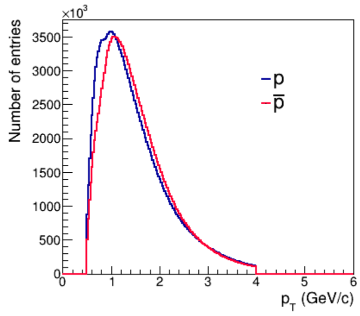

Figure 5.47: Transverse momentum distribution for Run 3 data.

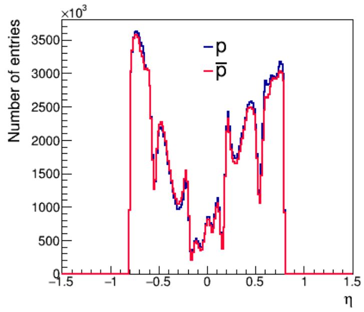

Figure 5.48: η distribution for Run 3 data.

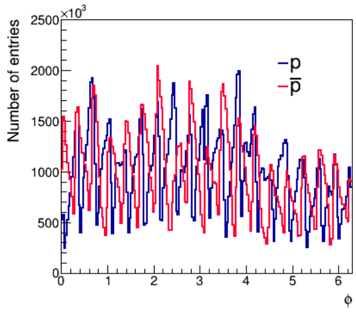

Figure 5.49: φ distribution for Run 3 data.

The $\frac{dE}{dx}$ signal from TPC shown in Fig. 5.50 and Fig. 5.53 looks clear with protons and antiprotons selected well, however both the TPC n_σ and TOF n_σ distributions presented in Fig. 5.51, Fig. 5.52, Fig. 5.54 and Fig. 5.55 are shifted towards higher values instead of centered at 0. This again is the result of data still being in reconstruction, but since the majority of particles fall into the chosen cut, it can be an acceptable state for the time being.

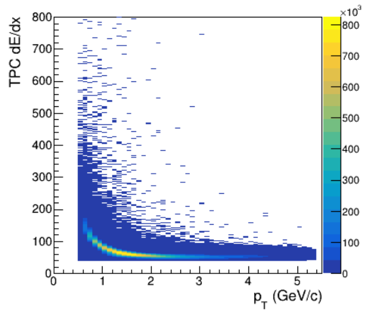

Figure 5.50: The TPC signal as a function of p_T for p from Run 3 data.

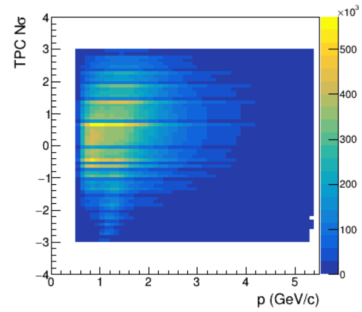

Figure 5.51: TPC n_σ distribution for p from Run 3 data.

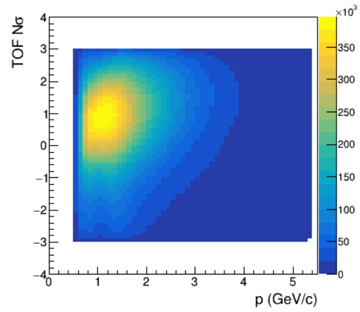

Figure 5.52: TOF n_σ distribution for p from Run 3 data.

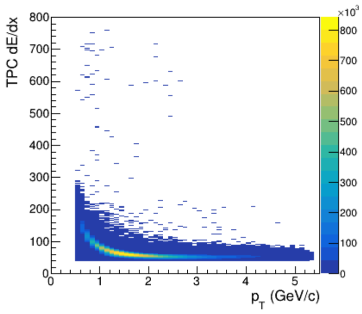

Figure 5.53: The TPC signal as a function of p_T for $\bar{p}$ from Run 3 data.

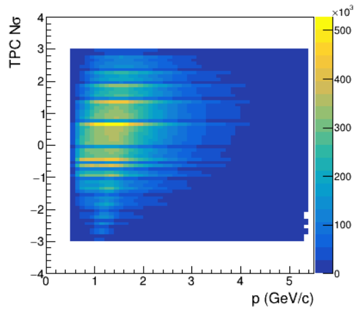

Figure 5.54: TPC n_σ distribution for $\bar{p}$ from Run 3 data.

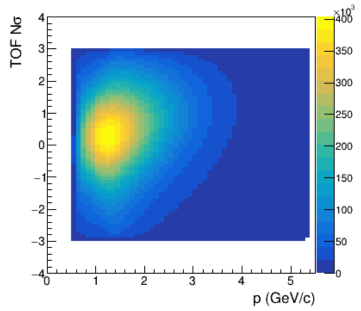

Figure 5.55: TOF n_σ distribution for $\bar{p}$ from Run 3 data.

Proton and antiproton purity was calculated using MC data anchored to the newest runs. It also may contain some flaws, being the first one available, but it should, to some degree, provide reliable depiction of the selection. In Fig. 5.56 purity dependence is shown in relation to p_T. It is significantly lower than for previous runs, especially for antiprotons. At around $p_T = 1\ \frac{\text{GeV}}{\text{c}}$ there is a large decrease, falling as low as 50%. At this p_T range, it is a possible contamination from kaons that comes into play. Integrated purity is presented in table 5.2.

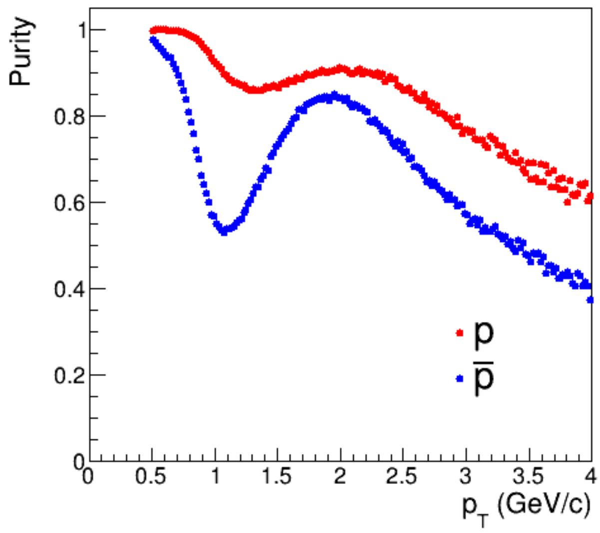

Figure 5.56: p and $\bar{p}$ purity for 2023 data from LHC23k6c_pass1 MC PYTHIA simulations.

p purity	$\bar{p}$ purity
98.84%	98.60%

Table 5.2: Integrated purity for Run 3 data.

5.4.2. Correlation function

As centrality reconstruction was not available for the largest dataset form the 2023 period at the time of writing thesis, only full correlation was calculated to ensure better statistics. In Fig. 5.57 the pair distributions from the same and mixed events can be seen. As event mixing was performed in multiplicity, they don't experience the problem with wrong numerator and denominator proportions. The correlation function in Fig. 5.58 displays similar properties as seen before. It falls with lower k^* values due to annihilation between p and $\bar{p}$ and raises up at the last two bins as a result of Coulomb attraction. Some distortions are visible between the $0.03 < k^* < 0.11 \frac{\text{GeV}}{\text{c}}$ region possibly influenced by some contamination or flaw in reconstruction.

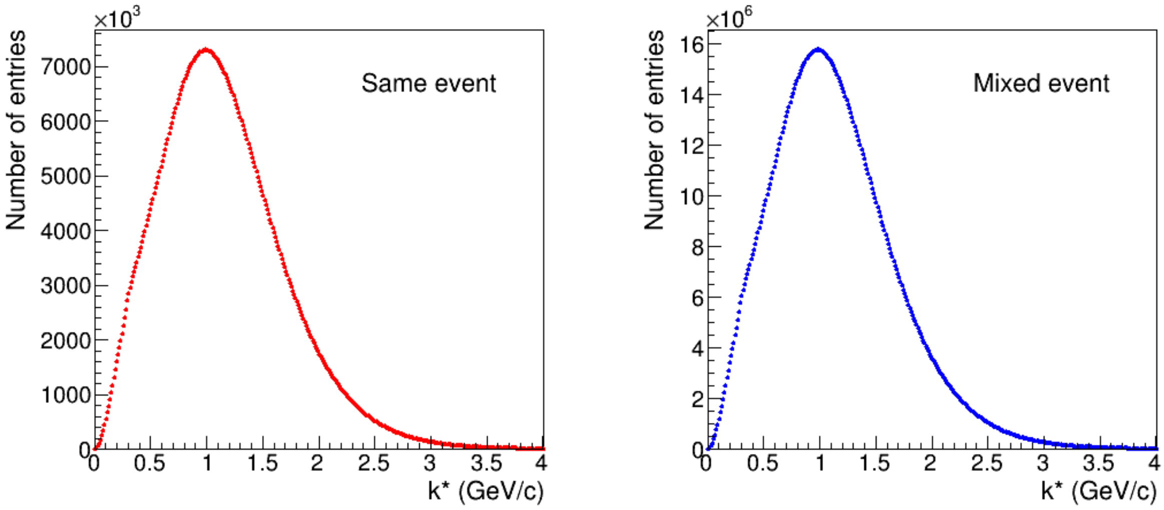

Figure 5.57: $p\bar{p}$ pair distributions coming from the same and different events from 2013 data.

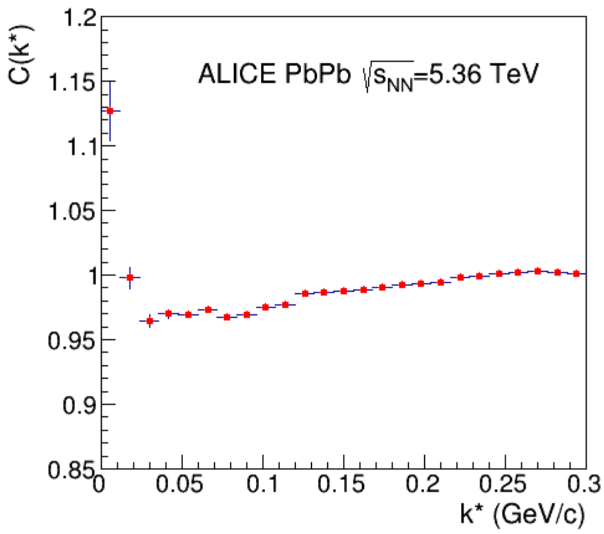

Figure 5.58: $p\bar{p}$ correlation from 2023 data.

Chapter 6

Summary

This thesis' primary goal was to analyse proton–antiproton femtoscopic correlations obtained from Pb–Pb collisions at $\sqrt{s_{\mathrm{NN}}} = 5.02$ TeV using the O^2 framework. Acquired results would mostly serve as a baseline for further studies of baryon-antibaryon interactions. With new Run 3 Pb–Pb collision data ready to be studied, it will be possible to observe change in results brought by higher collision rates, larger energies and better detection technology.

Code developed as part of my work, lays foundation for studying data from heavy–ion collision in the FemtoUniverse package in the O^2 framework, as well as helps perform reliable quality assurance using experimental data and Monte Carlo simulations. All new code has been used on datasets from Run 2 and Run 3, ensuring continuity of results between run periods. Performing QA analysis on new MC and experimental data was especially important to give experts feedback on the quality of reconstruction and to quickly find any possible flaws.

The $p\bar{p}$ femtoscopic analysis gave anticipated results. Despite the current problems with event mixing, it was possible to observe centrality, as well as k_T dependence of correlation effects. Results were compared with different multiplicity classes and was discovered, that they give very similar results. Comparison with published results form previous runs, suggests that the change of framework had little impact on observed physical effects. Difference in elliptic flow poses an interesting question of dependence on collision energy, but to come to a definite conclusion, analysis in identical k_T should be performed.

The last part of the analysis focused on new data from 2023 Pb–Pb run period. The QA calculations show that data reconstruction still requires improvement to get reliable results for femtoscopic analysis. Even though the sample may have contained some degree of contamination from other particles, a preliminary correlation function was calculated showing very similar femtoscopic effects as for Run 2 data.

Further study of the $p\bar{p}$ correlations should include fitting theoretical functions and removing background effects using Monte Carlo simulations. The same procedure may be followed for Run 3 data when final reconstruction is available, thus allowing to study interactions at higher energies and collision rates. This would lay foundation for studying more complex baryon–antibaryon systems including much less explored $\Lambda\bar{\Lambda}$ correlations.

Bibliography

[1] W. Busza, K. Rajagopal and W. van der Schee. *Heavy Ion Collisions: The Big Picture and the Big Questions*. *Annual Review of Nuclear and Particle Science*, 68(1):339–376, 2018.

[2] L. Evans and P. Bryant. *LHC Machine*. *Journal of Instrumentation*, 3(S08001), 2008.

[3] *Heavy–ion collision*. `https://cds.cern.ch/record/2789548/plots`, accessed: 13.12.2023.

[4] M. A. Lisa, S. Pratt, R. Soltz and U. Wiedemann. *Femtoscopy in relativistic heavy ion collisions: Two decades of progress*. *Annual Review of Nuclear and Particle Science*, 5(1), 2005.

[5] S. E. Koonin. *Proton pictures of high-energy nuclear collisions*. *Physics Letters B*, 70(1):43–47, 1977.

[6] T. Csörgő, S. Pratt and J. Zimányi. *Detailed predictions for two-pion correlations in ultrarelativistic heavy-ion collisions*. *Physical Review C*, 42:2646–2652, Dec 1990.

[7] A. Kisiel. *Non–identical particle correlation analysis in the presence of non–femtoscopic correlations*. *Acta Physica Polonica B*, 48(4), 2017.

[8] ALICE Collaboration. *Measurement of strange baryon–antibaryon interactions with femtoscopic correlations*. *Physics Letters B*, 802:135223, 2020.

[9] *About CERN*. `https://home.cern/about/who-we-are`, accessed: 1.08.2023.

[10] *The CERN accelerator complex*. `https://cds.cern.ch/record/2197559`, accessed: 1.08.2023.

[11] ALICE Collaboration et al. *The ALICE experiment at the CERN LHC*. *Journal of Instrumentation*, 3(08):S08002, 2008.

[12] M. Bernardini and K. Foraz. *Long Shutdown 2 at LHC*. *Proceedings of the Chamonix 2014 Workshop on LHC Performance*, 2, 2015.

[13] J. Adolfsson et al. *The upgrade of the ALICE TPC with GEMs and continuous readout*. *Journal of Instrumentation*, 16(03):P03022, 2021.

[14] F. Reidt. *Upgrade of the ALICE ITS detector*. *Nuclear Instruments and Methods in Physics Research Section A: Accelerators, Spectrometers, Detectors and Associated Equipment*, 1032:166632, 2022.

[15] W. H. Trzaska. *New ALICE detectors for Run 3 and 4 at the CERN LHC*. *Nuclear Instruments and Methods in Physics Research Section A: Accelerators, Spectrometers, Detectors and Associated Equipment*, 958:162116, 2020. Proceedings of the Vienna Conference on Instrumentation 2019.

[16] *Fundamental Principles and Methods of Particle Detection*. In L. C. L. Yuan and C.-S. Wu, editors, *Nuclear Physics*, volume 5 of *Methods in Experimental Physics*, pages 1–288. Academic Press, 1961.

[17] *The upgraded ALICE TPC*. `https://ep-news.web.cern.ch/upgraded-alice-tpc`, accessed: 8.11.2023.

[18] A. Akindinov et al. *Performance of the ALICE Time-Of-Flight detector at the LHC*. *The European Physical Journal Plus*, 128(44), 2013.

[19] *Signal from the TPC detector*. `https://alice-doc.github.io/alice-analysis-tutorial/analysis/pid.html`, accessed: 20.08.2023.

[20] N. Jacazio. *PID performance of the ALICE-TOF detector in Run 2. Proceedings of Sixth Annual Conference on Large Hadron Collider Physics*, 2018.

[21] *The O^2 documentation.* `https://aliceo2group.github.io/analysis-framework/docs/gettingstarted/`, accessed: 24.09.2023.

[22] *The C++ standard.* `https://isocpp.org/`, accessed: 6.01.2024.

[23] *Apache Arrow.* `https://arrow.apache.org/`, accessed: 6.01.2024.

[24] *ALICE Collaboration GitHub repository.* `https://github.com/AliceO2Group`, accessed: 25.01.2024.

[25] *Code for efficiency and purity analysis in the O^2 framework.* `https://github.com/AliceO2Group/O2Physics/blob/737e417b01e6c5b3b8d8af73a89baca15ef4729d/PWGCF/FemtoWorld/Tasks/femtoWorldEfficiencyTask.cxx`, accessed: 26.01.2024.

[26] *FemtoUniverse Producer task in the O^2 framework.* `https://github.com/AliceO2Group/O2Physics/blob/737e417b01e6c5b3b8d8af73a89baca15ef4729d/PWGCF/FemtoUniverse/TableProducer/femtoUniverseProducerTask.cxx`, accessed: 26.01.2024.

[27] R. Quishpe, J. F. Grosse-Oetringhaus, R. Cruceru and C. Grigoras. *Hyperloop – The ALICE analysis train system for Run 3. Proceeding of Science*, LHCP2021:250, 2021.

[28] *Worldwide LHC Computing Grid.* `https://wlcg-public.web.cern.ch`, accessed: 24.09.2023.

[29] *AliPhysics documentation.* `http://alidoc.cern.ch/AliPhysics/master/`, accessed: 25.01.2023.

[30] X. N. Wang and M. Gyulassy. *HIJING: A Monte Carlo model for multiple jet production in pp, pA and AA collisions. Physical Review D*, 44(11), 1991.

[31] C. Bierlich, S. Chakraborty, N. Desai, L. Gellersen, I. Helenius, P. Ilten, L. Lönnblad, S. Mrenna, S. Prestel, C. T. Preuss, T. Sjöstrand, P. Skands, M. Utheim and R. Verheyen. *A comprehensive guide to the physics and usage of PYTHIA 8.3. SciPost Physics Codebases*, page 8, 2022.

[32] A. Maevskaya and ALICE Collaboration. *ALICE FIT data processing and performance during LHC Run 3. Physics of Atomic Nuclei*, 84:579–584, 2021.

[33] M. Szymański and A. Kisiel. *Two-proton correlations in Pb–Pb collisions at $\sqrt{s_{NN}} = 2.76$ TeV from the ALICE experiment at the LHC.* 2015. analysis note, access restricted for ALICE Collaboration members.

List of Figures

List of Tables

Appendix A

List of runs

A.1. LHC15o

244917, 244918, 244975, 244980, 244982, 244983, 245064, 245066, 245068, 245145, 245146, 245151, 245152, 245231, 245232, 245233, 245259, 245343, 245345, 245346, 245347, 245349, 245353, 245396, 245397, 245401, 245407, 245409, 245410, 245411, 245439, 245441, 245446, 245450, 245452, 245453, 245454, 245496, 245497, 245501, 245504, 245505, 245507, 245535, 245540, 245542, 245543, 245544, 245545, 245554, 245683, 245692, 245700, 245702, 245705, 245729, 245731, 245738, 245752, 245759, 245766, 245775, 245785, 245793, 245829, 245831, 245833, 245923, 245949, 245952, 245954, 245963, 246001, 246003, 246012, 246036, 246037, 246042, 246048, 246049, 246052, 246053, 246087, 246089, 246113, 246115, 246148, 246151, 246152, 246153, 246178, 246180, 246181, 246182, 246185, 246217, 246222, 246225, 246271, 246272, 246275, 246276, 246390, 246391, 246392, 246424, 246428, 246431, 246434, 246675, 246676, 246750, 246751, 246757, 246758, 246759, 246760, 246763, 246765, 246766, 246804, 246805, 246807, 246808, 246809, 246810, 246844, 246845, 246846, 246847, 246851, 246858, 246859, 246864, 246865, 246867, 246870, 246871, 246928, 246945, 246948, 246980, 246982, 246984, 246989, 246991, 246994.

A.2. LHC_18q_PbPb

295585, 295586, 295587, 295588, 295589, 295610, 295611, 295612, 295615, 295665, 295666, 295667, 295668, 295673, 295675, 295676, 295677, 295712, 295714, 295717, 295718, 295719, 295721, 295723, 295725, 295753, 295754, 295755, 295756, 295758, 295759, 295762, 295763, 295786, 295788, 295791, 295816, 295818, 295819, 295822, 295825, 295826, 295829, 295831, 295853, 295854, 295855, 295856, 295859, 295860, 295861, 295881, 295908, 295909, 295910, 295913, 295936, 295937, 295941, 295942, 295943, 295945, 295947, 296016, 296060, 296061, 296062, 296063, 296065, 296066, 296068, 296074, 296123, 296132, 296133, 296134, 296135, 296142, 296143, 296191, 296192, 296194, 296195, 296196, 296197, 296198, 296240, 296241, 296242, 296243, 296244, 296246, 296247, 296269, 296270, 296273, 296279, 296280, 296303, 296304, 296307, 296309, 296312, 296375, 296376, 296377, 296378, 296379, 296380, 296381, 296383, 296414, 296415, 296419, 296420, 296423, 296424, 296433, 296472, 296509, 296510, 296511, 296512, 296514, 296516, 296547, 296548, 296549, 296550, 296551, 296552, 296553, 296594, 296615, 296616, 296618, 296619, 296621, 296622, 296623.

A.3. LHC_18r_PbPb

296690, 296691, 296693, 296694, 296749, 296750, 296752, 296781, 296784, 296785, 296786, 296787, 296790, 296793, 296794, 296799, 296835, 296836, 296838, 296839, 296848, 296849, 296850, 296851, 296852, 296890, 296894, 296899, 296900, 296903, 296930, 296931, 296932, 296934, 296935, 296938, 296941, 296966, 297029, 297031, 297035, 297085, 297117, 297118, 297119, 297123, 297124, 297128, 297129, 297132, 297133, 297193, 297194, 297195, 297196, 297218, 297219, 297221, 297222, 297278, 297310, 297311, 297312, 297315, 297317, 297332, 297333, 297335, 297336, 297363, 297366, 297367, 297372, 297379, 297380, 297405, 297406, 297413, 297414, 297415, 297441, 297442, 297446, 297450, 297451, 297452, 297479, 297481, 297483, 297512, 297537, 297540, 297541, 297542, 297544, 297558, 297588, 297590, 297595.

A.4. LHC20f6

244918, 244980, 244982, 244983, 245061, 245064, 245066, 245068, 245145, 245146, 245148, 245151, 245152, 245231, 245232, 245259, 245343, 245345, 245346, 245347, 245349, 245353, 245396, 245397, 245401, 245407, 245409, 245410, 245411, 245439, 245441, 245446, 245450, 245452, 245454, 245496, 245497, 245501, 245504, 245505, 245507, 245535, 245540, 245542, 245543, 245544, 245554, 245683, 245692, 245700, 245702, 245705, 245729, 245731, 245738, 245752, 245759, 245766, 245775, 245785, 245793, 245829, 245831, 245833, 245923, 245952, 245954, 245963, 246001, 246003, 246012, 246037, 246042, 246048, 246049, 246052, 246053, 246087, 246089, 246113, 246115, 246148, 246151, 246152, 246153, 246178, 246180, 246181, 246182, 246185, 246217, 246222, 246225, 246271, 246272, 246275, 246276, 246390, 246391, 246392, 246424, 246428, 246431, 246434, 246487, 246488, 246493, 246495, 246553, 246575, 246583, 246648, 246675, 246676, 246750, 246751, 246757, 246758, 246759, 246760, 246763, 246765, 246804, 246805, 246807, 246808, 246809, 246810, 246844, 246845, 246846, 246847, 246851, 246865, 246867, 246870, 246871, 246928, 246945, 246948, 246980, 246982, 246984, 246989, 246991, 246994.

A.5. LHC20e3c

295585, 295586, 295587, 295588, 295589, 295610, 295611, 295612, 295615, 295665, 295666, 295667, 295668, 295671, 295673, 295675, 295676, 295677, 295712, 295714, 295717, 295718, 295719, 295721, 295723, 295725, 295753, 295754, 295755, 295756, 295758, 295759, 295762, 295763, 295786, 295788, 295791, 295816, 295818, 295819, 295822, 295825, 295826, 295829, 295831, 295853, 295854, 295855, 295856, 295859, 295860, 295861, 295881, 295908, 295909, 295910, 295913, 295936, 295937, 295941, 295942, 295943, 295945, 295947, 296016, 296060, 296061, 296062, 296063, 296065, 296066, 296068, 296074, 296123, 296132, 296133, 296134, 296135, 296142, 296143, 296191, 296192, 296194, 296195, 296196, 296197, 296198, 296240, 296241, 296242, 296243, 296244, 296246, 296247, 296269, 296270, 296273, 296279, 296280, 296303, 296304, 296307, 296309, 296312, 296375, 296376, 296377, 296378, 296379, 296380, 296381, 296383, 296414, 296415, 296419, 296420, 296423, 296424, 296433, 296472, 296509, 296510, 296511, 296512, 296514, 296516, 296547, 296548, 296549, 296550, 296551, 296552, 296553, 296594, 296615, 296616, 296618, 296619, 296621, 296622, 296623, 296690, 296691, 296693, 296694, 296749, 296750, 296752, 296781, 296784, 296785, 296786, 296787, 296790, 296793, 296794, 296799, 296835, 296836, 296838, 296839, 296848, 296849, 296850, 296851, 296852, 296890, 296894, 296899, 296900, 296903, 296930, 296931, 296932, 296934, 296935, 296938, 296941, 296966, 297029, 297031, 297035, 297085, 297117, 297118, 297119, 297123, 297124, 297128, 297129, 297132, 297133, 297193, 297194, 297195, 297196, 297218, 297219, 297221, 297222, 297278, 297310, 297311, 297312, 297315, 297317, 297332, 297333, 297335, 297336, 297363, 297366, 297367, 297372, 297379, 297380, 297405, 297406, 297413, 297414, 297415, 297441, 297442, 297446, 297450, 297451, 297452, 297479, 297481, 297483, 297512, 297537, 297540, 297541, 297542, 297544, 297558, 297588, 297590, 297595.

A.6. LHC20e3c

544091, 544095, 544098.